Ocean Engineering 195 (2020) 106678

Contents lists available at ScienceDirect

Ocean Engineering

journal homepage: www.elsevier.com/locate/oceaneng

A numerical toolbox for wave-induced seabed response analysis around marine structures in the OpenFOAM® framework

Yuzhu Li [a], Muk Chen Ong [a,*], Tian Tang [b]

[a] Department of Mechanical and Structural Engineering and Materials Science, University of Stavanger, N-4036 Stavanger, Norway
[b] Bekaert Technology Center, Deerlijk, 8540, Belgium

ARTICLE INFO

Keywords:
Wave-structure-seabed interaction
Numerical solver
Consolidation
Momentary liquefaction

ABSTRACT

An open-source numerical toolbox for modeling the porous seabed interaction with waves and structures is implemented in the finite-volume-method (FVM) based OpenFOAM® framework. The toolbox includes a soil consolidation model, a wave-structure-seabed interaction (WSSI) model, and the liquefaction assessment module. In the present work, one-way coupling algorithm is applied for the WSSI analysis. The coupling effect between different physical domains is achieved by time-varying data mapping via the common boundaries. The consolidation model is governed by the quasi-static Biot's equations and is verified against the theoretical solution for the Terzaghi's classical consolidation test. The anisotropic wave-induced porous seabed response model is governed by the Biot's equations in the partial-dynamic form, i.e. $u-p$ approximation form, to achieve a good efficiency and accuracy. The FVM-based $u-p$ model is validated against the existing experimental data of standing wave-induced seabed response near a vertical wall. The integrated WSSI model is validated against existing experiment of wave-soil-pile interaction with wave data and soil response data. Good agreement is obtained. Two case studies are performed using the present numerical toolbox. The first case is an investigation of two-dimensional (2D) nonlinear wave-seabed interaction. The second case is a three-dimensional (3D) parametric study of wave-induced seabed response analysis around gravity-based offshore foundations with various designs. The 3D parametric study follows the sequence of consolidation analysis, WSSI analysis and liquefaction assessment. Two types of liquefaction criteria are implemented and compared in the present study. The toolbox is made publicly available through the foam-extend community.

1. Introduction

For offshore foundations and coastal structures, soil liquefaction is one of the essential concerns which may cause the structural failure. In order to prevent the liquefaction risk around the offshore foundations and coastal structures, the investigation of wave-induced seabed response in the vicinity of the structures is important. The modeling of the interaction problem incorporating multiple physical domains including the fluid domain of waves and the solid domain(s) of the seabed (and the structure).

To date, most of the studies in the open literature followed the manner of using the volume of fluid (VOF) method or boundary element method (BEM) to solve the wave domain and a separate code or software based on the finite element method (FEM) or finite difference method (FDM) to solve the soil domain (Ye, 2012b; Jeng et al., 2013; Zhang et al., 2015; Sui et al., 2016). For example, Jeng et al. (2013) proposed a model for the wave-induced seabed response around marine structures. In their work, the VOF method is applied to model the waves and the FEM is applied for the soil analysis. However, to couple different numerical methods/tools for each physical domain, the external data exchange and time-step update can incur a high usage of computational memory and a low efficiency. Jeng (2012) reviewed the numerical methods for wave-seabed interaction in terms of FDM (Zen and Yamazaki, 1990a, b; Sui et al., 2019), FEM (Okusa, 1985; Gatmiri, 1990; Jeng and Hsu, 1996; Jeng and Lin, 2000) and BEM (Raman-Nair et al., 1991), respectively. Among them, the FEM method has been most commonly used. In recent years, with the development of open-source software, the FVM-based OpenFOAM becomes a platform for multiphysics solver development. Using the same numerical method within the same framework, the time and computational memory required by the data exchange between different physical domains can be reduced. Liu et al. (2007) first discretized the Biot's equations in an FVM manner within

* Corresponding author.
E-mail address: muk.c.ong@uis.no (M.C. Ong).

https://doi.org/10.1016/j.oceaneng.2019.106678
Received 28 August 2018; Received in revised form 31 August 2019; Accepted 2 November 2019
Available online 31 December 2019

OpenFOAM. They investigated the wave-induced response around submerged objects but without parallel computing. Tang et al. (2014) implemented a three-dimensional FVM-based anisotropic poro-elastic Biot's model in the quasi-static form. The quasi-static anisotropic poro-elastic solver by Tang et al. (2014) was validated and applied in the work of Li et al. (2018) in which the anisotropic consideration was proved to be practical for modeling the seabed of medium and coarse sand. Elsafti and Oumeraci (2016) developed a hydro-geotechnical solver named *geotechFoam* to model the soil-structure interaction around the marine gravity structures, including a multi-yield surface plasticity model to simulate plastic soil response under cyclic loads. The soil constitutive model for simulating plastic deformations and two-dimensional wave loading on the elastic seabed without a structure has been validated in their work. However, the interaction of waves, the seabed and the marine structure has not been modelled and validated and liquefaction analysis has not been conducted in their work. Based on previous studies, the present toolbox is developed to investigate the interaction of nonlinear waves, the anisotropic poro-elastic seabed and the marine structure and further to assess the wave-induced momentary liquefaction risk around the marine structures in the OpenFOAM framework.

The natural seabed sand experiences the 'wave-induced compaction' (Sumer, 2014a) for a long history. Under cyclic loading, the loose soil will experience the built up and then dissipation of the pore pressure. The loose soil particles will rearrange the relative positions to a more dense status. For the natural seabed in a dense status due to the long history of 'wave-induced compaction' process, the poro-elastic theory and momentary (instantaneous) liquefaction analysis can provide satisfactory results (Ye et al., 2015). The present study focuses on the investigation of momentary liquefaction in the poro-elastic seabed. However, in some offshore areas, there might exist newly deposited loose sand soil which is typical elastoplastic soil so that a poro-elastoplastic soil model should be utilized (Ye and Wang, 2016). As pointed in Ye et al. (2015), this kind of sand soil has a weak bearing capability and is easy to liquefy under cyclic loading. Therefore, it is risky to build the marine structures upon it. Also, in some fields, when the seabed is active due to continuous sediment transport with sand waves so that the soil is constantly being reworked, residual liquefaction can be encountered. In the work of Ulker et al. (2009b) and Ulker et al. (2010), three forms of the Biot's poro-elastic soil model were discussed, in terms of the quasi-static form, the partial dynamic form (i.e., the $u-p$ formulation), and the fully dynamic form. The difference between the forms is based on the consideration of including inertial terms associated with the motion of fluids and solids. The fully dynamic Biot's model contains the terms associated with the acceleration of the soil and relative acceleration of the fluid compared to the soil. However, it was reported that the fully dynamic solution could provide a good prediction but the solutions were lengthy and difficult to be applied in engineering practice, as discussed in the work of Jeng and Rahman (2001) and Jeng and Cha (2003). The $u-p$ approximation model was proposed by Zienkiewicz et al. (1980) based on Biot's poro-elastic theory (Biot, 1956). The pore fluid acceleration relative to the solid phase is neglected, in order to reduce the computational effort compared to the fully dynamic form. The $u-p$ formulation can be more accurate than the quasi-static form for the dynamic cases with moderate frequencies. It also reduces the computational effort compared to the fully dynamic form of the Biot's model.

The present work implements the $u-p$ approximation Biot's model in the FVM-based framework with anisotropic considerations. The finite volume (FV) soil solver is named anisoUpFoam and is coupled with FV wave solver and structure solver to investigated the WSSI interaction. The present FV $u-p$ model is validated against experimental data of standing wave-induced pore pressure in the soil by Tsai and Lee (1995). To validate the integrated WSSI analysis model, the experiment of wave-pile-soil interaction (Qi and Gao, 2014; Qi, 2018) is reproduced. The experimental data used in this work were not presented in the paper of Qi and Gao (2014). Through personal contact with Qi (2018), the unpublished data were used in the present work to validate the WSSI model.

To analyze the liquefaction risk in the seabed, the assessment of soil consolidation behavior in the presence of marine structures is essential. A consolidation solver named elasticBiotConsolidationFoam in the quasi-static form accounting for the gravitational forces of the marine structure is developed in the present work. The consolidation solver is verified against the theoretical solution for the one-dimensional Terzaghi's consolidation test by Wang (2017). For the liquefaction analysis, various liquefaction criteria have been proposed based on the effective stress (Tsai, 1995; Okusa, 1985) or the excess pore pressure (Zen and Yamazaki, 1990b; Jeng, 1997). The liquefaction assessment module in the present toolbox incorporates the proposed criteria based on both the vertical effective stress and the excess pore pressure.

The present toolbox is then applied to two case studies. The first one is a 2D nonlinear wave-seabed interaction case without the presence of the structure. In the second one, a 3D parametric study of wave-induced seabed response investigation around offshore foundations with various designs is carried out, following the sequence of consolidation analysis, WSSI analysis and liquefaction assessment. Two liquefaction criteria are applied and compared.

The toolbox can be used to investigate the seabed response and liquefaction risk around offshore foundations and marine structures in waves. It is built with a series of solvers and utilities, including a consolidation solver, an anisotropic soil response solver with liquefaction assessment module, a linear structural response solver, and interface data mapping utilities. Each specific solver requires minimized parameter specification and can be used independently for the specific analysis of consolidation or soil response. Parallel running is allowed for each solver. The present FVM model can model arbitrary 3D geometry of the structure. Using parallel running, a large domain can be solved in a fast manner. The toolbox is made publicly available through the foam-extend community (Li et al., 2019).

2. Theoretical background

2.1. Free surface wave model

In the wave-structure-seabed analysis, the wave domain is governed by the incompressible Navier-Stokes equations including the continuity equation and the momentum equations.

$$\nabla \cdot \mathbf{u} = 0 \tag{1}$$

$$\frac{\partial \mathbf{u}}{\partial t} + (\mathbf{u} \cdot \nabla)\mathbf{u} = -\frac{1}{\rho_f}\nabla p_d + \mathbf{g} + \frac{1}{\rho_f}\nabla \cdot \boldsymbol{\tau} \tag{2}$$

where $\mathbf{u}$ denotes the velocity vector with three components in the x,y, and z directions respectively; $\mathbf{g}$ denotes the gravitational acceleration; ρ_f is the fluid density which can represent the air ρ_a or the water ρ_w. p_d is the dynamic wave pressure which is defined as $p_d = p_t - \rho_f \mathbf{g}\cdot\mathbf{x}$, where p_t is the total pressure and the $\mathbf{x} = (x, y, z)$ is the Cartesian coordinate vector. $\boldsymbol{\tau}$ is the viscous stress tensor with Einstein notation of τ_{ij}. For Newtonian fluid,

$$\tau_{ij} = 2\mu\sigma_{ij} \tag{3}$$

where μ is the dynamic molecular viscosity with μ_{air} for the air and μ_{water} for the water. σ_{ij} is defined by

$$\sigma_{ij} = \frac{1}{2}\left(\frac{\partial u_i}{\partial x_j} + \frac{\partial u_j}{\partial x_i}\right) \tag{4}$$

where $i, j \in [1,2,3]$. u_i and u_j denote the velocity components in x, y and z direction, respectively.

The equations are solved for the two immiscible fluids simulta-

neously, where the fluids are tracked using a scalar field α. α is 0 for air and 1 for water, and any intermediate value is a mixture of the two fluids. The distribution of α is modelled by an advection equation

$$\frac{\partial \alpha}{\partial t} + \nabla \cdot \alpha \mathbf{u} + \nabla \cdot [\alpha(1-\alpha)\mathbf{u}_r] = 0 \tag{5}$$

The last term on the left-hand side is a compression term, which limits the smearing of the interface, and $\mathbf{u}_r$ is a relative velocity (Berberović et al., 2009).

Using α, one can express the spatial variation in any fluid property, through the weighting

$$\Phi = \alpha \Phi_{water} + (1-\alpha)\Phi_{air} \tag{6}$$

Φ is a fluid property, such as ρ_f and μ.

2.2. Linear elastic structure model

The structure domain is modelled as a linear elastic media and is governed by a linear momentum balance equation and isotropic linear elastic strain-displacement relations. The equations and the solving of the equations can be referred to Li et al. (2018).

2.3. Anisotropic Biot's consolidation model

In the present work, the soil behavior is modelled by the classical Biot's consolidation equations (Biot, 1941) with the interaction between the solid skeleton and the pore fluids, considering the anisotropic soil characteristics. The seabed is nearly saturated and the soil skeleton generally obeys Hooke's law with elastic properties.

2.3.1. Constitutive relations

In the present work, the tension stress is defined as positive while the compression stress is defined as negative, in compliance with the tradition in computational continuum mechanics. The total stress for the saturated porous medium is defined by

$$\boldsymbol{\sigma} = \boldsymbol{\sigma}^{'} - p\mathbf{I} \tag{7}$$

where $\boldsymbol{\sigma}^{'}$ is the effective stress tensor of the soil skeleton, $\boldsymbol{\sigma}$ is the total stress tensor of soil mixture, p is the pore fluid pressure, and $\mathbf{I}$ is the identity tensor.

Effective stress-strain relation by the generalized Hooke's law is expressed as

$$\boldsymbol{\sigma}^{'} = C : \boldsymbol{\varepsilon} \tag{8}$$

The strain-displacement relation is expressed as

$$\boldsymbol{\varepsilon} = \frac{1}{2}\left(\nabla \mathbf{U} + (\nabla \mathbf{U})^T\right) \tag{9}$$

where $\boldsymbol{\varepsilon}$ is the strain tensor, $\mathbf{U}$ is the soil skeleton displacement vector.

For anisotropic soil materials, the orthotropic elastic stress-strain relation can be expressed in a 6 × 6 matrix notation:

$$\boldsymbol{\sigma}^{'} = \begin{pmatrix} \sigma_{xx}^{'} \\ \sigma_{yy}^{'} \\ \sigma_{zz}^{'} \\ \sigma_{xy} \\ \sigma_{yz} \\ \sigma_{xz} \end{pmatrix} = \begin{bmatrix} A_{11} & A_{12} & A_{31} & 0 & 0 & 0 \\ A_{12} & A_{22} & A_{23} & 0 & 0 & 0 \\ A_{31} & A_{23} & A_{33} & 0 & 0 & 0 \\ 0 & 0 & 0 & A_{44} & 0 & 0 \\ 0 & 0 & 0 & 0 & A_{55} & 0 \\ 0 & 0 & 0 & 0 & 0 & A_{66} \end{bmatrix} \begin{pmatrix} \varepsilon_{xx} \\ \varepsilon_{yy} \\ \varepsilon_{zz} \\ \varepsilon_{xy} \\ \varepsilon_{yz} \\ \varepsilon_{xz} \end{pmatrix} = \mathbf{C} : \boldsymbol{\varepsilon} \tag{10}$$

where $\boldsymbol{\sigma}^{'}$ is the effective stress tensor. According to the work of Demirdžić et al. (2000), the 9 independent coefficients A_{ij} are calculated from Young's modulus E_i and Poisson's ratio ν_{ij} and shear modulus G_{ij} as follows:

$$\begin{aligned} A_{11} &= \frac{1-\nu_{yz}\nu_{zy}}{JE_yE_z}, & A_{22} &= \frac{1-\nu_{xz}\nu_{zx}}{JE_xE_z}, & A_{33} &= \frac{1-\nu_{yx}\nu_{xy}}{JE_yE_x}, \\ A_{12} &= \frac{\nu_{xy}+\nu_{zy}\nu_{xz}}{JE_xE_z}, & A_{23} &= \frac{\nu_{yz}+\nu_{yx}\nu_{xz}}{JE_xE_y}, & A_{31} &= \frac{\nu_{zx}+\nu_{yx}\nu_{zy}}{JE_yE_z}, \\ A_{44} &= 2G_{xy}, & A_{55} &= 2G_{yz}, & A_{66} &= 2G_{zx} \end{aligned} \tag{11}$$

where

$$J = \frac{1-\nu_{xy}\nu_{yx}-\nu_{yz}\nu_{zy}-\nu_{xz}\nu_{zx}-2\nu_{yx}\nu_{zy}\nu_{xz}}{E_xE_yE_z} \tag{12}$$

2.3.2. Quasi-static model for consolidation analysis

The Biot's model contains two governing partial differential equations:

(i) One vector equation for the momentum equilibrium.
(ii) One scalar equation for the mass conservation.

In the consolidation analysis, a static gravitational force is imposed on the seabed; therefore, the Biot's model in the quasi-static form is applied because the frequency of the process is very low. The soil domain in the consolidation analysis is governed by a quasi-static momentum balance equation for the soil mixture and a mass balance equation for the pore fluid based on Darcy's law. The quasi-static momentum balance equation is presented in Eqn. (13):

$$\nabla \cdot \left[\mathbf{C} : \frac{1}{2}\left(\nabla \mathbf{U} + (\nabla \mathbf{U})^T\right)\right] - \nabla p + \rho \mathbf{g} = 0 \tag{13}$$

where $\mathbf{U}$ is the soil (skeleton) displacement, p is the pore fluid pressure, ρ is the density of the soil mixture, $\mathbf{g}$ is the gravitational acceleration vector with components of $(0, 0, g)$, and $\mathbf{C}$ is the fourth-order elastic stiffness tensor. The density of the soil mixture, or submerged density of the soil is calculated by

$$\rho = n\rho_f + (1-n)\rho_s \tag{14}$$

where n is the porosity, ρ_s is the soil density and ρ_f is the water density.

The mass balance equation of the pore fluid based on Darcy's law is shown in Eqn. (15):

$$\frac{n}{K^{'}}\frac{\partial p}{\partial t} - \frac{1}{\gamma_w}\nabla \cdot (\mathbf{k} \cdot \nabla p) + \frac{\partial}{\partial t}(\nabla \cdot \mathbf{U}) + \frac{\mathbf{k}}{g} \cdot (\nabla \cdot \mathbf{g}) = 0 \tag{15}$$

where n denotes the soil porosity, γ_w denotes the specific weight of water in soil, and $\mathbf{k}$ denotes the diagonal permeability tensor with values of k_x, k_y and k_z. The bulk modulus of the compressible pore flow $K^{'}$ is approximately computed by using the formulation of Vafai and Tien (1981):

$$\frac{1}{K^{'}} = \frac{1}{K_w} + \frac{1-S_r}{p_a} \tag{16}$$

where S_r denotes the degree of soil saturation, K_w denotes the bulk modulus of pure water (≈ 2 GPa), and $p_a = \rho_f g h_w$ denotes the absolute pore water pressure at the seabed.

2.3.3. u-p approximation model for wave-induced seabed response

The partial dynamic $u-p$ formulation is more accurate compared to the quasi-static form for the oscillating problems and is more efficient compared to the fully-dynamic form for most of the engineering problems. Therefore, it is adopted for the wave-induced seabed response modeling in the present work. Satisfactory accuracy has been reported by the previous work such as Ye et al. (2013a).

The wave-induced soil response analysis starts from the status that the gravity structure has been installed in place and the consolidation process has been completed. At this stage, the seabed soil has adjusted

itself in equilibrium with the massive weight of the gravity structure. The governing equations for the $u-p$ approximation model to analyze the wave effect on the soil is given as follows:

$$\nabla\cdot\left[\mathbf{C}:\frac{1}{2}\left(\nabla\mathbf{U}+(\nabla\mathbf{U})^{T}\right)\right]-\nabla p-\rho\frac{\partial^{2}\mathbf{U}}{\partial t^{2}}=0 \tag{17}$$

$$\frac{n}{K^{'}}\frac{\partial p}{\partial t}-\frac{1}{\gamma_{w}}\nabla\cdot(\mathbf{k}\cdot\nabla p)+\frac{1}{g}\nabla\cdot\left(\mathbf{k}\cdot\frac{\partial^{2}\mathbf{U}}{\partial t^{2}}\right)+\frac{\partial}{\partial t}(\nabla\cdot\mathbf{U})=0 \tag{18}$$

It is noted that the gravitational term $\rho\mathbf{g}$ is not incorporated in Eqn. (17) for the force balance. It is because that the partial dynamic $u-p$ approximation form is applied for the pure wave-induced soil response analysis, which starts from an equivalent status between the structure and the soil. Therefore, in Eqn. (17), the external force is only the dynamic wave pressure, incorporated in the term p.

2.4. Liquefaction criteria

As mentioned before, there are various liquefaction criteria in the open literature based on the effective stress (Tsai, 1995; Okusa, 1985) or the excess pore pressure (Zen and Yamazaki, 1990b; Jeng, 1997). Ye (2012a) compared different liquefaction criteria for the seabed without marine structure built on it. Ye (2012a) concluded that among those liquefaction criteria based on the effective stress, the criteria of Okusa (1985) provides most appropriate engineering solution and among those liquefaction criteria based on the excess pore pressure, the criteria of Zen and Yamazaki (1990b) provide the best engineering solution.

However, these criteria and the conclusion drawn in Ye (2012a) are all applicable to the cases without a structure. In the case of liquefaction around a gravity structure, the initial effective stress from the consolidation stage should be taken into consideration. In the present work, following modified liquefaction criteria considering the presence of the structure are incorporated in the liquefaction assessment module, including:

(i) Criterion A. The modified form from Okusa (1985),

$$\sigma_{z}^{'}\geq\left|\sigma_{z0}^{'}\right| \tag{19}$$

where $\sigma_{z0}^{'}$ is the initial vertical effective stress induced by the gravitational forces from the consolidation process. The applications of this criterion can be referred to the work of Jeng et al. (2013) and Ye et al. (2014).

(ii) Criterion B. The modified form from Zen and Yamazaki (1990b),

$$p-p_{b}\geq\left|\sigma_{z0}^{'}\right| \tag{20}$$

where p_b is the wave-induced pressure on the seabed surface. The applications of this criterion can refer to the work of Sui et al. (2017), Zhao et al. (2017) and Sui et al. (2019).

The right hand sides of Eqn. (19) and Eqn. (20) express the downward gravitational forces including the soil weight and the external gravitational forces. The left hand sides of the liquefaction equations express the upward wave-induced hydraulic forces. In the present work, the two liquefaction criteria above are implemented. The present study will evaluate and compare the two representative criteria (A and B) in the application section (Section 5) with a gravity-based structure built on the seabed. It is worthwhile to mention that in the presence of the structure, especially when the structure is constructed on the loose seabed soil, nonlinear interaction between the seabed and the structure can occur. Therefore, the present liquefaction criteria can be no longer applicable. It is reported in Ye and Wang (2015) that when the structure was built on newly deposited Quaternary sediment seabed, it could sink, tilt and rotate under seismic loading resulting from liquefaction and softening of the seabed soil. They found that the upward pore pressure gradient generated near the structure could exceed the initial vertical effective stress even if the soil was not fully liquefied. It is because the stress state of the surrounding soil was significantly affected during the soil-structure interaction process after the ground shaking. In the present work, it is assumed that the seabed can provide a valid support to the structure before the instantaneous liquefaction occurs. Therefore, there is no soil-structure interaction involved in the present model.

2.5. Finite volume method based approach

In the Biot's model, the momentum and mass balance equations are strongly coupled. In the FVM analysis, the coupling of the three displacement components U_x, U_y, U_z and pressure p are handled by using a 'segregated strategy' (Demirdžić and Martinović, 1993; Demirdžić and Muzaferija, 1994). The equations are split into the 'implicit' and 'explicit' discretization parts, where the 'explicit' parts contain all the coupling effect from the other variables and shall be evaluated from the previous iteration or the initial condition.

The cross-component coupling in Eqn. (10) can be decomposed into implicit and explicit components:

$$\boldsymbol{\sigma}^{'}=\mathbf{C}:\boldsymbol{\varepsilon}=\underbrace{\mathbf{K}\cdot\nabla\mathbf{U}}_{\text{implicit}}+\underbrace{\mathbf{C}:\boldsymbol{\varepsilon}-\mathbf{K}\cdot\nabla\mathbf{U}}_{\text{explicit}}. \tag{21}$$

where the $\mathbf{K}$ is a 3×3 diagonal stiffness tensor given by

$$\mathbf{K}=\begin{bmatrix}A_{11}&0&0\\0&A_{22}&0\\0&0&A_{33}\end{bmatrix} \tag{22}$$

In this way, Eqn. (13) and Eqn. (15) can be rearranged into the FVM implicit-explicit format:

$$\underbrace{\nabla\cdot(\mathbf{K}\nabla\mathbf{U})}_{\text{implicit}}=\underbrace{\nabla\cdot\left[\mathbf{C}:\frac{1}{2}\left(\nabla\mathbf{U}+\nabla\mathbf{U}^{T}\right)\right]+\nabla\cdot(\mathbf{K}\nabla\mathbf{U})-\nabla p+\rho\mathbf{g}}_{\text{explicit}} \tag{23}$$

$$\underbrace{\frac{n}{K^{'}}\frac{\partial p}{\partial t}-\frac{1}{\gamma_{w}}\nabla\cdot(\mathbf{k}\cdot\nabla p)}_{\text{implicit}}=\underbrace{-\frac{\partial}{\partial t}(\nabla\cdot\mathbf{U})-\frac{\mathbf{k}}{g}\cdot(\nabla\cdot\mathbf{g})}_{\text{explicit}} \tag{24}$$

Similarly, the FVM implicit-explicit format for the $u-p$ approximation model to apply to the wave effect analysis is written as:

$$\underbrace{\nabla\cdot(\mathbf{K}\nabla\mathbf{U})}_{\text{implicit}}=\underbrace{\nabla\cdot\left[\mathbf{C}:\frac{1}{2}\left(\nabla\mathbf{U}+\nabla\mathbf{U}^{T}\right)\right]+\nabla\cdot(\mathbf{K}\nabla\mathbf{U})-\nabla p-\rho\frac{\partial^{2}\mathbf{U}}{\partial t^{2}}}_{\text{explicit}} \tag{25}$$

$$\underbrace{\frac{n}{K^{'}}\frac{\partial p}{\partial t}-\frac{1}{\gamma_{w}}\nabla\cdot(\mathbf{k}\cdot\nabla p)}_{\text{implicit}}=\underbrace{-\frac{\partial}{\partial t}(\nabla\cdot\mathbf{U})-\frac{1}{g}\nabla\cdot\left(\mathbf{k}\cdot\frac{\partial^{2}\mathbf{U}}{\partial t^{2}}\right)}_{\text{explicit}} \tag{26}$$

The iterative procedure for solving the Biot's models are shown in Fig. 1. Equations are solved iteratively until the solution changes less than a pre-defined tolerance. As pointed out in the work of Jasak and Weller (2000), the finite-volume (FV) discretization to the linear stress analysis problem uses small matrices for the three components of displacement, rather than using one large matrix that seen in the FEM. In this way, the usage of the computer memory can be significantly reduced.

3. The Fvm-based wssi toolbox

3.1. The solvers

The present FVM-based toolbox can be applied to soil consolidation analysis, WSSI analysis, and liquefaction assessment. An outline of the toolbox and an illustration of the systematic analysis procedure is

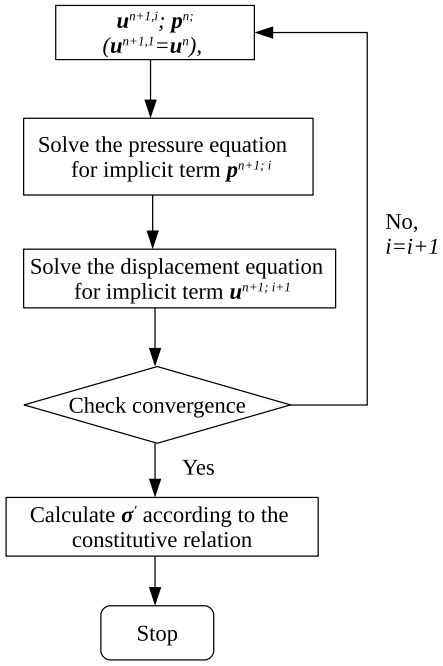

Fig. 1. Iteration procedure for solving the Biot's model.

presented in Fig. 2. The present toolbox reads wave pressure data from a free-surface solver. There is no restriction on selecting the free-surface modeling tools. In the OpenFOAM CFD library, various solvers can be adopted, such as interFoam solver in OpenFoam®, toolboxes of waves2Foam (Jacobsen et al., 2012) and iHFoam (Higuera et al., 2013). In the present work, the waves2Foam is adopted for modeling the wave generation and absorption.

For the soil consolidation analysis, the new solver named biotConsolidationFoam is developed in the present work. It reads the static gravitational force from the structure and computes the initial vertical effective stress in the soil. In the WSSI analysis, the new solver named anisoUpFoam is developed to consider the anisotropic soil property and the inertial force of the soil skeleton. For the liquefaction assessment, a module is developed to read data from the consolidation analysis and the WSSI analysis. Criteria extended from Okusa (1985) and Zen and Yamazaki (1990a) are implemented. Since the toolbox is based on the poro-elastic soil model, the momentary liquefaction is assessed.

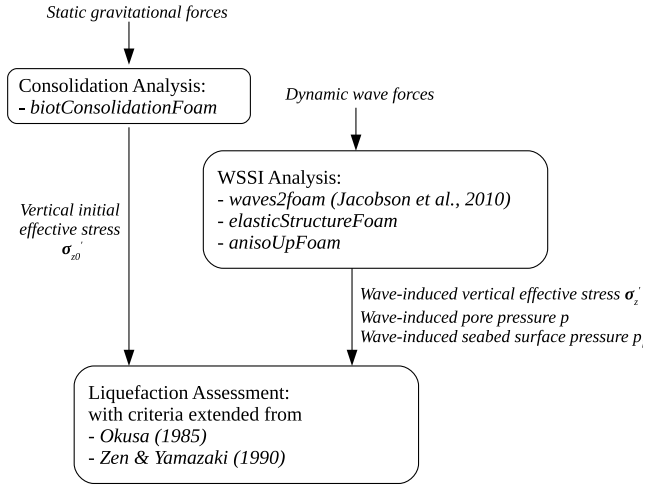

Fig. 2. An outline of the FVM-based WSSI toolbox.

3.2. Boundary conditions

3.2.1. Boundary conditions for consolidation analysis

Boundary conditions for consolidation analysis are presented in Fig. 3a. In the consolidation analysis, the static gravitational force from the structure $-\sigma_0$ is read as the boundary condition at the structure-seabed interface. In the present case, the static stress at the structure bottom is calculated as

$$-\sigma_0 = -(W-B)/A \tag{27}$$

where W is the weight of the structure, B is the buoyant force and A is the area of the structure-seabed interface. However, for structures with more complicated geometry where the stress on the bottom of structure is not uniform, the present model allows users to input the non-uniform gravity-induced stress/pressure distribution at the structure bottom.

A Neumann type boundary for the displacement at the structure-seabed interface is specified with a traction-displacement relation $\nabla\mathbf{U} = \mathrm{f}(\mathbf{T})$. The traction $\mathbf{T}$ is defined by

$$\mathbf{T} = \boldsymbol{\sigma}\cdot\mathbf{n} \tag{28}$$

where $\mathbf{n}$ is the surface normal vector. The traction-displacement relation is expressed as

$$\mathbf{T} = \left[\mu\nabla\mathbf{U} + \mu(\nabla\mathbf{U})^T + \lambda\mathbf{I}tr(\nabla\mathbf{U})\right]\cdot\mathbf{n} \tag{29}$$

Therefore, a displacement gradient boundary can be derived from Eqn. (29) as

$$(\nabla\mathbf{U})\cdot\mathbf{n} = \frac{\mathbf{T} - [\mu(\nabla\mathbf{U})^T + \lambda\mathbf{I}tr(\nabla\mathbf{U}) - (\mu+\lambda)\nabla\mathbf{U}]\cdot\mathbf{n}}{(2\mu+\lambda)} \tag{30}$$

The term $[\mu(\nabla\mathbf{U})^T + \lambda\mathbf{I}tr(\nabla\mathbf{U}) - (\mu+\lambda)\nabla\mathbf{U}]$ on the right-hand side is treated explicitly. Iterations are used to compute the compatible displacement gradient $(\nabla\mathbf{U})$ with known $\mathbf{T}$.

At the seabed surface, a zero-traction boundary is specified where $\mathbf{T} = 0$. A static water pressure $p = \rho_f g h_w$ is applied on the seabed boundary. At the seabed bottom, the pore pressure p has zero normal gradient and the displacement is zero. At the seabed lateral sides, the pore pressure p has zero normal gradient. A slip boundary is specified at the seabed lateral sides for the displacement where the normal displacement to the boundary U_n is zero.

3.2.2. Boundary conditions for WSSI analysis

In the dynamic WSSI analysis, one-way coupling algorithm is considered, due to the small magnitudes of wave-induced structure vibration and soil deformation compared to the wavelength. The one-way coupling (semi-coupled) method was firstly proposed by Ye et al. (2013b). The time-varying data transfer in a single direction at the interfaces, i.e., from waves to the structure, from waves to the seabed and from the structure to the seabed. The small structure and seabed motions do not alter the wave domain. The dynamic wave pressure p_d imposes directly on the seabed through the wave-seabed interface and imposed indirectly on the seabed through wave-structure and structure-seabed interfaces. The schematic one-way coupling procedure for the dynamic WSSI analysis and the corresponding boundary conditions are presented in Fig. 3b.

Boundary conditions for wave modeling are specified as follows.

- The inlet velocity is specified as the input wave velocity $\mathbf{u} = \mathbf{u}_0$, while the outlet velocity is $\mathbf{u} = 0$. The pressure at the inlet and outlet has zero normal gradient.
- At four sides of the numerical wave tank, the pressure has zero normal gradient. A slip boundary is set for the velocity at the lateral sides where the flow is passing along the walls and the normal flow velocity u_n is zero.

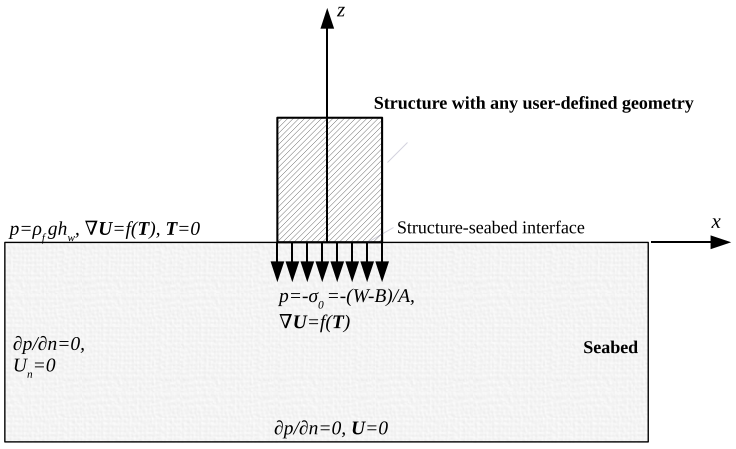

(a) Boundary conditions of the consolidation analysis.

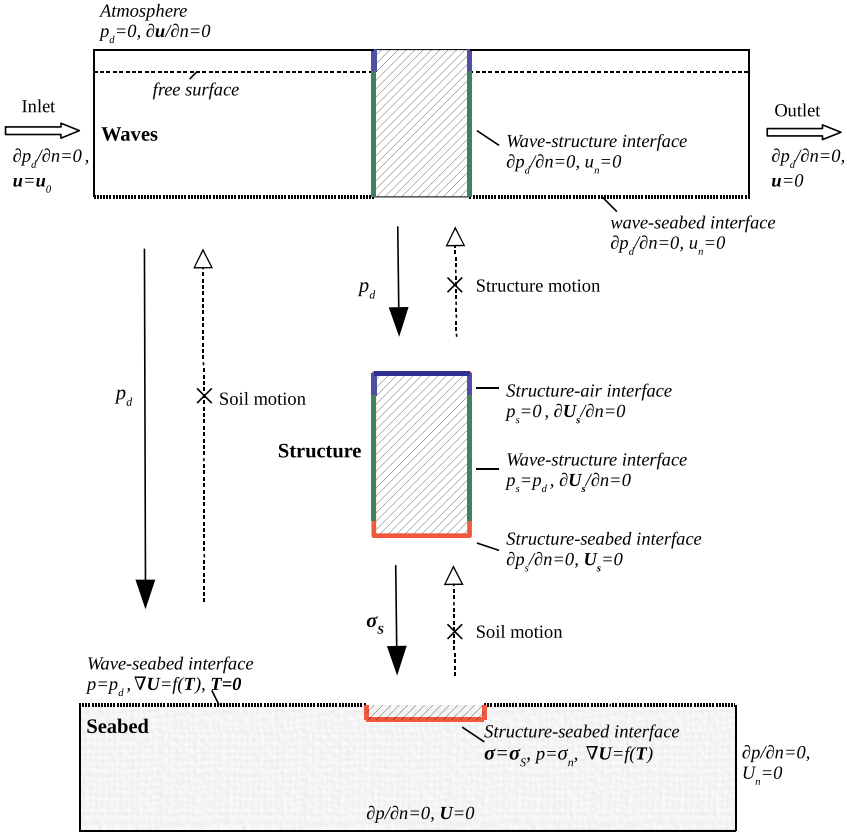

(b) Boundary conditions of wave-structure-seabed interaction (WSSI) model and the one-way boundary coupling algorithm.

Fig. 3. Boundary conditions of consolidation analysis and wave-structure-seabed interaction (WSSI) analysis.

- At the atmosphere, the dynamic wave pressure p_d is zero and the velocity has zero normal gradient.
- At the wave-structure interface and the wave-seabed interface, the pressure has zero normal gradient. A slip boundary is set for the velocity. Bottom boundary layer effect is neglected since it has insignificant effect on the dynamic wave pressure results.

Boundary conditions for structure analysis are specified as follows.

- At the structure-air interface, the dynamic pressure on the structure is zero. The structure displacement U_s has zero gradient.
- At the wave-structure interface, the dynamic pressure p_s is read from the dynamic wave pressure p_d. The structure displacement has zero normal gradient.

- At the structure-seabed interface, the dynamic pressure p_s has zero normal gradient. The structure displacement is set to zero based on the assumption that the structure is rigid and the seabed can provide a valid support to the structure.

Boundary conditions for seabed analysis are specified as follows.

- At the wave-seabed interface, the soil has zero traction. The displacement boundary at the wave-seabed interface is computed via the traction-displacement relation. The pore pressure is equal to the dynamic wave pressure on the seabed.
- At the structure-seabed interface, the pore pressure has zero normal gradient since the structure is impermeable. The soil displacement at the structure-seabed interface is triggered by the structural force, while the structural force is wave-induced. The displacement boundary at the structure-seabed interface is also computed via the traction-displacement relation.
- At the lateral sides of the seabed, the pore pressure has zero normal gradient. The soil skeleton is allowed to slip.
- At the seabed bottom, the pore pressure has zero normal gradient. The soil skeleton has zero displacement.

For solving the multiphysics WSSI problems, different physical domains can have different demands on the time step and grid size, based on the convergence and stability requisitions. For the WSSI problem, the time steps and the grid sizes needed for the linear-elastic soil and structural domains are relatively larger than what is needed for the nonlinear wave domain (Li, 2016). Therefore, it not efficient to calculate the multiple domains with the same grid size and to loop at the same time step. In the model proposed by Ye et al. (2013b), a larger minimum grid size of the soil model than that of the wave model was also used. In the present model, time-dependent (time-varying) boundary conditions are applied for the data mapping at the interfaces. First, the values at the interfaces of the supplied domain are interpolated in space and time. Then, the interpolated values are mapped to the targeted domain interface with a reversed normal vector. In the present work, linear interpolation is applied. The boundary data are first interpolated in space for every face center and then interpolated linearly between the time instants.

4. Validation and verification

4.1. Verification of the FV Biot's consolidation solver

The present FV consolidation solver is verified against Terzaghi's classical consolidation test (Terzaghi, 1944; Wang, 2017). In Terzaghi's classical consolidation test, a constant stress $-\sigma_0$ is applied suddenly on the surface $z = 0$ of a saturated sample of length L_s. Here, z is positive in the downward direction. The piston applying the load is permeable so that the top boundary is drained. The sample consolidates gradually as fluid flows out from the top drain. The setup of the test is shown in Fig. 4. The input parameters for the present numerical simulation is presented in Table 1.

The boundary conditions for reproducing the test is specified as follows:

At $z = 0$,

$$\sigma_z = -\sigma_0, p = 0 \tag{31}$$

At $z = L_s$,

$$\frac{\partial p}{\partial z} = 0, u_z = 0 \tag{32}$$

At four sides of the column, the boundary condition is defined as 'empty', i.e., the x and y directions are not solved, to achieve a one-dimensional problem.

Wang (2017) provided the non-dimensional analytical solutions for

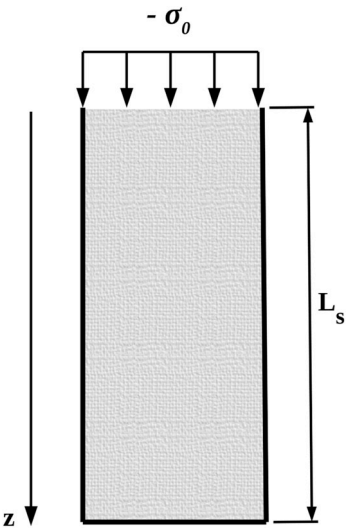

Fig. 4. Test setup of Terzaghi's classical consolidation test.

Table 1
Parameter setting in the present numerical simulation for the 1D Terzaghi's consolidation test.

Parameters	Values
L_s (m)	20
σ_0 (kPa)	10
Permeability k (m/s)	10^{-5}
Youngs modulus E (N/m^2)	10^8
Saturation degree S_r	0.995
Poisson's ratio ν	0.25
Porosity n	0.3

Terzaghi's consolidation theory. Fig. 5a and Fig. 5b show the comparison of pore pressure and vertical soil displacement between the present numerical results and the analytical solution at certain time instants during the consolidation process. The pressure p is normalized by the initial undrained response $p_0 = \Upsilon\sigma_0$, where Υ denotes the loading efficiency according to Wang (2017). Υ is 0.725 in the present simulation. The vertical soil displacement U is normalized by the sample length L_s. The time instant t is normalized by L_s^2/c where c is the hydraulic diffusivity that governs the time lag. As shown in Fig. 5a, under the constant stress, the soil is consolidated along the time. The excess pore pressure is dissipated gradually from time instant $ct/L^2 = 0.01$ to 1.0. The present numerical results are consistent with the analytical solutions in terms of the pore pressure distribution and the vertical soil displacement.

4.2. Validation of the FV $u-p$ approximation soil solver

The present FV $u-p$ approximation soil solver is validated against the experimental data of Tsai and Lee (1995). Their experiment investigated the standing waves induced pore pressure in the sand bed in the vicinity of a vertical wall. In the work of Li et al. (2018), the same experiment was adopted to validate the quasi-static Biot poro-elastic solver. The present work reproduces the experiment of Tsai and Lee (1995) by using the $u-p$ approximation soil solver. The present numerical results are compared with the experimental data of Tsai and Lee (1995) and the numerical results by the quasi-static Biot poro-elastic solver in Li et al. (2018).

The experimental setup by Tsai and Lee (1995) is shown in Fig. 6. Waves propagated to the sand bed region in a flume and reflected at a vertical smooth wall at the end of the wave flume. In the sand bed, nine pore pressure transducers were placed vertically and horizontally below

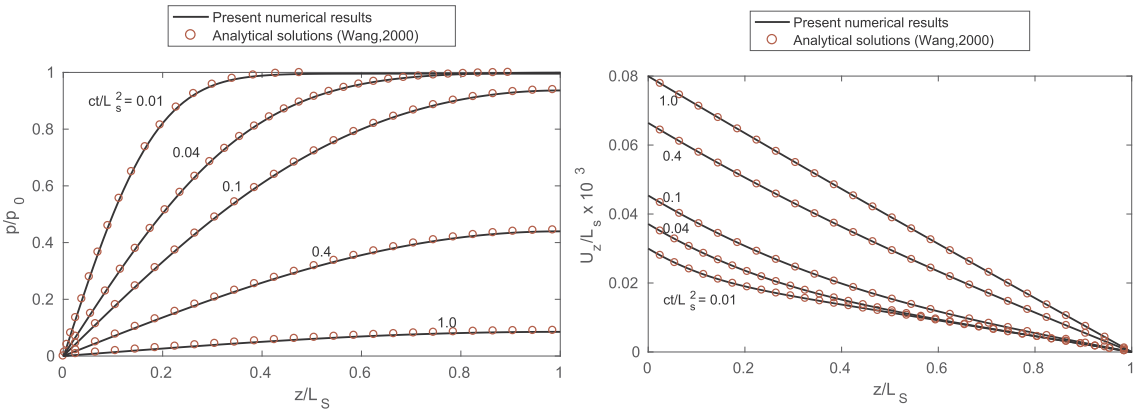

(a) Pore pressure distribution. (b) Vertical displacement.

Fig. 5. Verification of the consolidation model by comparing the present numerical results (biotConsolidationFoam) to the analytical solutions (Wang, 2017).

and close to the vertical wall, as shown in Fig. 6. Five of the pressure transducers were installed vertically below the wall from the sand bed surface with 10 cm distance in between. Another four were installed horizontally at a depth of 10 cm in the sand with distances of $kx = 1/10\pi$, $2/10\pi$, $3/10\pi$, $4/10\pi$ and $5/10\pi$ to the wall, where k is the wave number. The sand was in medium firmness and the properties are presented in Table 2. The present numerical simulation uses the second-order Stokes wave theory to model the propagating waves based on the given wave properties. The amplitude of pore pressure in the soil p_s is normalized by the amplitude of the pressure on the sand bed surface p_0. Fig. 7 shows the comparison of pore pressure in the seabed between the present numerical results and the experimental data. They are in good agreement.

The present numerical results of FV $u-p$ model is also compared with the numerical results of FV quasi-static model by Li et al. (2018), as shown in Fig. 8. It is seen that the present partial dynamic $u-p$ model gives slightly higher prediction of the pore pressure than the quasi-static model, and is closer to the experimental measurement. The difference between quasi-static model and $u-p$ model is not very significant in this case (with a maximum difference ratio of 8.6% at the sand bed bottom), due to the mild wave condition. Nevertheless, the $u-p$ model shows a better prediction than the quasi-static model for this experiment, as compared to the experimental measurement. In rough sea or breaking wave cases, the difference between two numerical models can be more significant due to higher acceleration (Ulker et al., 2009a). Since the predicted excess pore pressure by $u-p$ model is higher than the quasi-static model, the $u-p$ model is able to provide a more conservative solution for the engineering problems.

4.3. Validation of the WSSI model

The present WSSI model including FV $u-p$ approximation soil solver coupled with wave generation tool waves2Foam is validated against existing experimental data. Qi and Gao (2014) performed a series of experiments to investigate the local-scour and pore pressure responses around a large-diameter monopile in combined waves and current. In their work, the pore pressure and the time development of scour depth around the monopile under the conditions of wave-only, current-only and wave-plus-current were measured. However, in the paper of Qi and Gao (2014), only the experimental data under wave-plus-current and under current-only were presented. The experimental data under wave-only conditions provided by Qi (2018) are processed and presented in this work to validate the present WSSI numerical model. The test condition of the wave-only case is given in Table 3. The experimental set-up is shown in Fig. 9. Wave elevation data measured by three wave gauges are presented, with W1 in the far filed, W2 at 20 cm upstream to the pile and W3 at 10 cm upstream to the pile. Pore pressure data measured by four pressure gauges at two sides of the pile are presented. P1, P2 and P3 are located at the upstream side of the pile with 10 cm vertical gap in between. P4 is located at the downstream side of the pile. In view of the fact that the pile was installed before the sand box was filled in the experiment, the consolidation analysis is not required in the numerical reproduction of this experiment.

Comparisons of wave elevation and pore pressure between the present numerical simulation and the experimental data is shown in Fig. 10 and Fig. 11, respectively. Stokes second-order wave model is adopted for simulating the present waves. A good agreement is observed for the wave elevation results, with minor discrepancy in the wave trough amplitudes. The numerical results of the pore pressure also agree with the experimental data in the time series, with an average discrepancy of 6.9%. The present WSSI model is valid and is applicable to the case studies in Section 5.

Table 2
Physical properties of the wave and soil for model validation (experiment conducted by Tsai and Lee (1995)).

Wave parameters		Soil parameters			
Wave height H (cm)	5.1	Permeability k (m/s)	1.2×10^{-4}	Young's modules E (N/m^2)	6.86×10^{7}
Wave period T (s)	1.5	Porosity n	0.38	Shear modulus G (N/m^2)	2.64×10^{7}
Wave type	second-order	Poisson's ratio ν	0.3	Saturation degree S_r	0.98

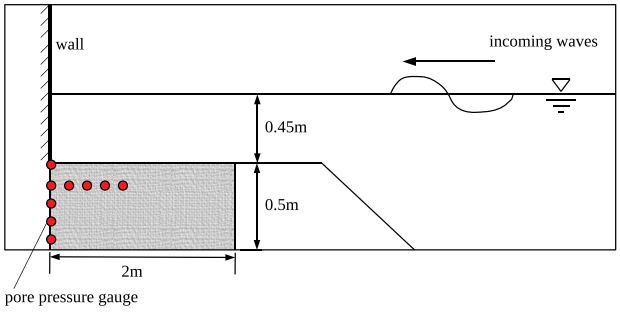

Fig. 6. Experimental setup of Tsai and Lee (1995).

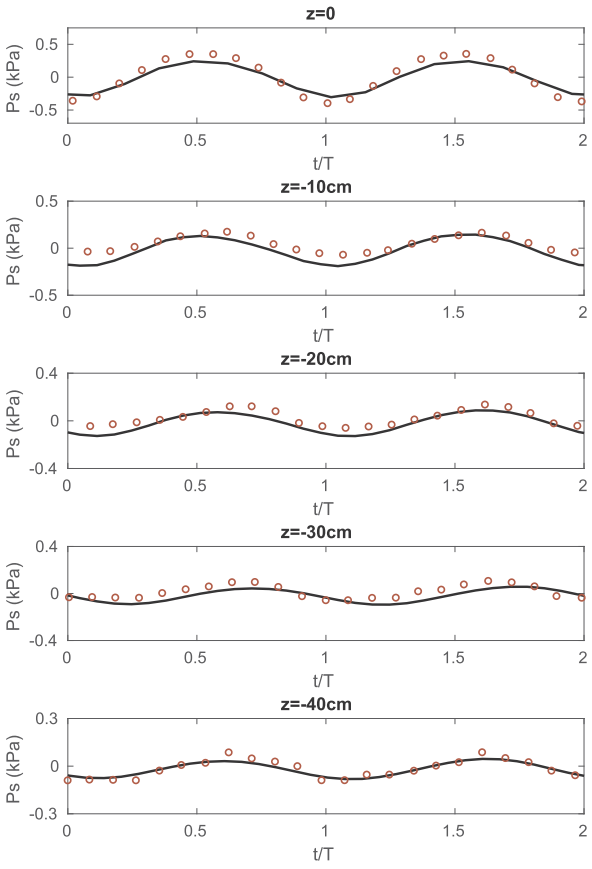

(a) Pore pressure at various depths, $kx = 0$.

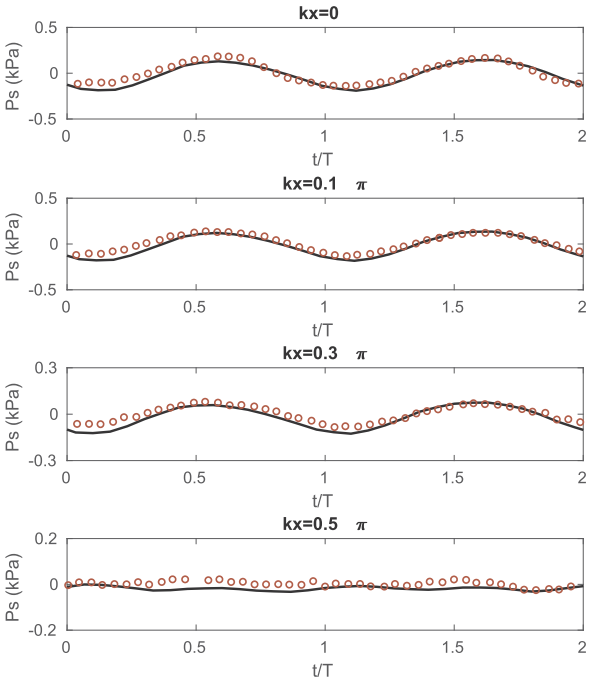

(b) Pore pressure at various horizontal positions, $z = -10$ cm.

Fig. 7. Comparisons of the pore pressure response between measured data by Tsai and Lee (1995) and the numerical results by present FV $u-p$ approximation solver (∘ : measured data by Tsai and Lee (1995); –: present numerical results by $u-p$ approximation solver.).

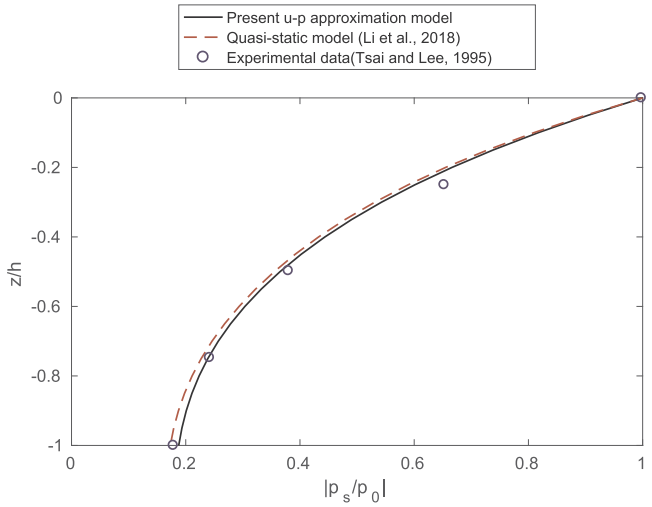

Fig. 8. Comparisons of the pore pressure at various depths, $kx = 0$.

5. Applications

5.1. Nonlinear wave-induced soil response

The present wssi toolbox is applied to investigate the wave-induced soil response with and without the presence of the structure. A case study of 2D nonlinear wave-induced soil response is performed with wave height $H = 0.5$ m, water depth $H_w = 3$ m and wave period $T = 2$ s.

Table 3
Parameter settings of the wave-pile-soil interaction experiment by Qi and Gao (2014).

Wave parameters	
Wave height H (cm)	5
Wave period T (s)	1.0
Water depth h_w (m)	0.5
Seabed parameters	
Seabed thickness d_s (m)	0.5
Young's modules E (N/m^2)	2.6×10^7
Poisson's ratio ν	0.3
Permeabilities (m/s) k	1.88×10^{-4}
Saturation factor S_r	0.997
Porosity n	0.435

According to the work of Fenton (1985), the fifth-order Stokes wave theory is applied to model the propagating waves considering the wave condition. A wave flume of 36-m long is simulated by using the OpenFoam wave generation tool waves2Foam with inlet and outlet relaxation techniques (Jacobsen et al., 2012) to ensure the accuracy and no influence from the reflected waves. The soil domain is 30-m long and 3-m thick. The soil parameters in the Tsai and Lee (1995)'s experiment, as shown in Table 2, are adopted with an anisotropic permeability consideration of $k_x = k_y = 5k_z = 6 \times 10^{-4}$ m/s. Fig. 12 (a) shows the dynamic wave pressure in the numerical wave flume and the pore pressure in the sand bed at a time instant of t/T = 15. When waves propagating over the and sand bed, a wave crest generates a positive

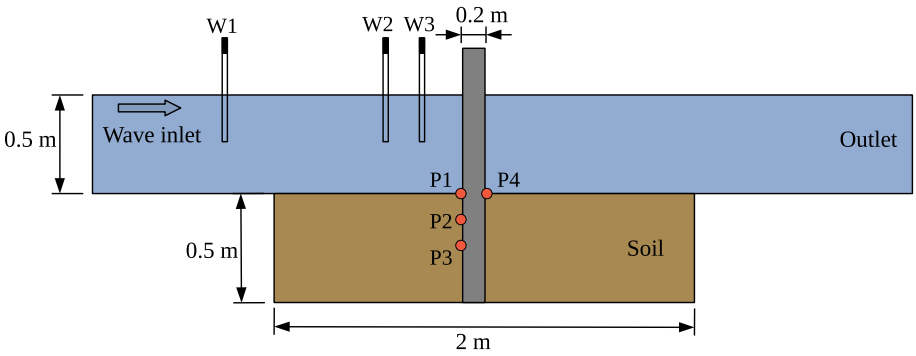

Fig. 9. Experimental set-up of wave-pile-soil interaction (Qi and Gao, 2014).

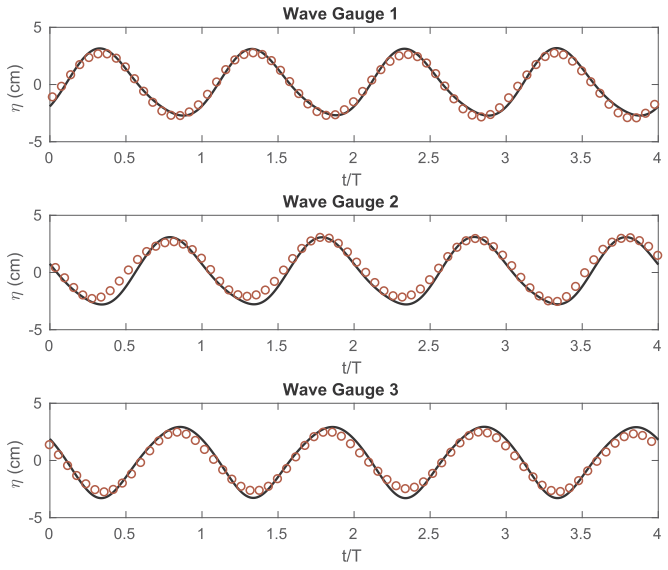

Fig. 10. Comparison of the wave elevation.

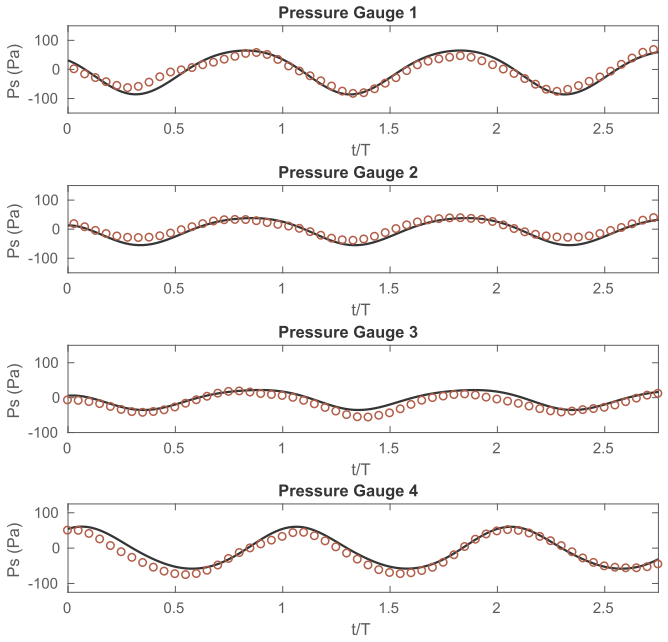

Fig. 11. Comparison of pore pressure around the pile.

pore pressure while a wave trough generates a negative pore pressure in the sand bed. The horizontal wave velocity field is presented in Fig. 12 (b) together with the vertical effective stress in the sand bed. The positive vertical effective stress (tension) results from the wave trough. Fig. 13 shows the time series of wave elevation and pore pressure in the sand bed. A phase-lag in the pore pressure diffusion is seen from a depth of 0–0.2 m in the sand bed. The phase-lag in the present case from sand bed surface to a 0.2-m depth is around one-sixth of the wave period. It has been proved that a phase lag exists in wave-induced soil response in a nearly saturated seabed of finite thickness (Jeng and Hsu, 1996) and also a cross-anisotropic seabed of infinite thickness (Jeng, 1998).

5.2. *Wave-structure-seabed interaction modeling for offshore foundations*

The integrated toolbox including the consolidation solver, WSSI solvers and the liquefaction module is applied to investigate the soil response and momentary liquefaction around offshore gravity-based foundations in a steep non-breaking wave condition. Gravity-based foundations for offshore wind turbines are normally installed close to the shore in a limited water depth. When waves travel into shallower water in the coastal areas, they are affected by the ocean bottom. The crest becomes higher and waves become steeper (Zhang et al., 2017). The gravity-based foundations are often exposed to steep waves while the linear wave theory is not applicable. Meanwhile, the gravity-based foundations have various designs that can result in different surrounding flow patterns and seabed pressure distributions after interacting with the incoming waves. The design of the gravity-based foundations usually consists of a slab (with a diameter D) and a shaft (with a diameter $D^{'}$) on top of it, as shown in Fig. 6. A different ratio of $D^{'}/D$ will directly affect the wave diffraction pattern and further affect the dynamic wave pressure and seabed response around the slab bottom. In this section, a parametric study on wave-structure-seabed interaction around gravity-foundations with different $D^{'}/D$ from 0.25 to 0.75 is performed. Simplified models of the gravity-based foundations are shown in Fig. 14b, while $D^{'}/D = 0.25$ resembles the diameter ratio of Lillgrund foundation in Jeppsson et al. (2008), $D^{'}/D = 0.5$ resembles the diameter ratio of the third generation of GBS concepts in Esteban et al. (2015). The slab height of $h_b = 0.189D$ is referred to the design of the Lillgrund foundation (Jeppsson et al., 2008). The design with $D^{'}/D = 1$ tends to be a monopile, which should be inserted into the seabed; therefore, it is not considered in the gravity-based circumstance. However, the $D^{'}/D = 1$ case is still computed in the present study to give a reference of the upper limit in the liquefaction risk assessment.

The numerical setup of the parametric study is shown in Fig. 14a. The entire system is built in a Cartesian coordinate system x, y, z, with $z = 0$ at the static free surface, x positive in the wave propagating direction, y positive toward the back of the tank, z positive upward. The width of the wave tank (distance between the sides of the tank) is set to be two wavelengths. Wave inlet and outlet relaxation zones (Jacobsen et al., 2012) are set to be 1 and 1.5 wave lengths, respectively. Wave

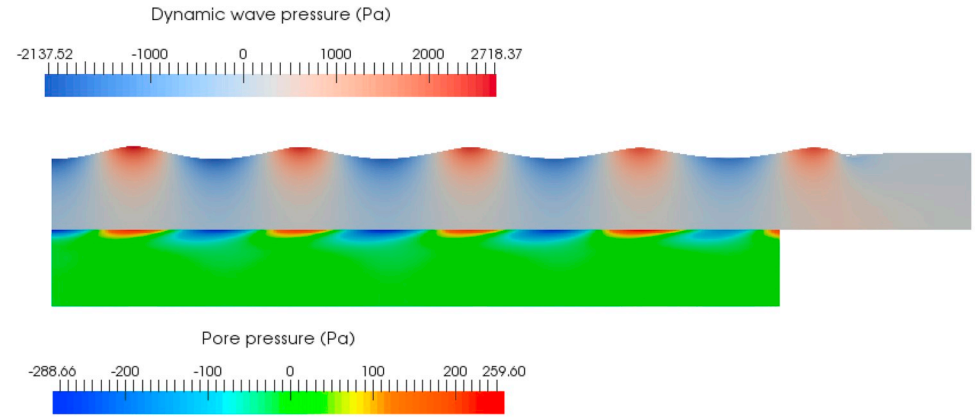

(a) Dynamic wave pressure in the wave flume and pore water pressure in the sand bed .

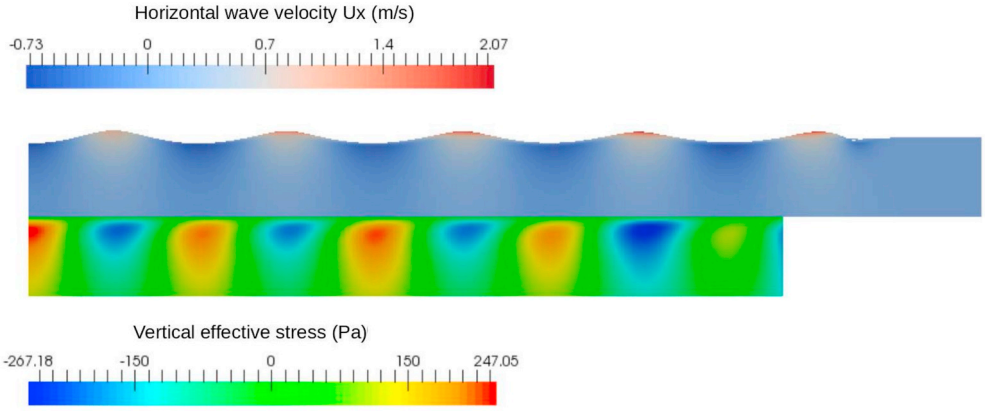

(b) Horizontal wave velocity in the wave flume and vertical effective stress in the sand bed.

Fig. 12. Numerical model of nonlinear wave-seabed interaction.

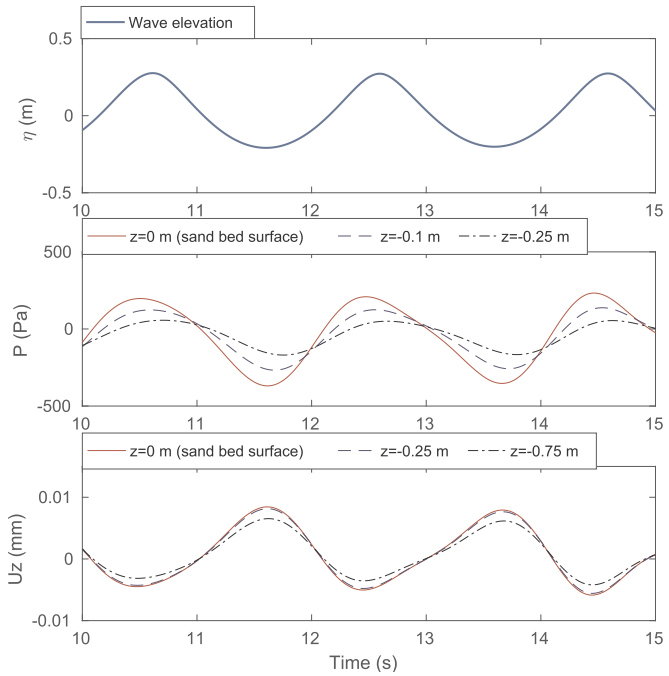

Fig. 13. Time series of wave elevation and the corresponding pore pressure in the sand bed.

parameters are set as follows. The wave steepness is $H/L = 0.095$. The relative water depth is $h_w/L = 0.175$ ($h_w/L \leq 0.1$ is considered as shallow water and $h_w/L \geq 0.5$ is considered as deep water). The water depth h_w is assumed as $1.75D$ and the corresponding wave length is $L = 10D$ and the wave height is $H = 0.95D$. Due to high nonlinearity of the incoming waves, 5th-order stream function wave theory (Dean, 1965) is utilized to model the waves. The structural material is considered as concrete with a density of 2400 kg/m^3. To examine the effect of $D^{'}/D$ of the foundation, the soil condition is kept constant. The seabed thickness is $d_s = 5D$. The soil property is referred to the measurement of the North sea soil by (Kjekstad and Lunne, 1981), with reasonable anisotropic considerations. The numerical parameters are given in Table 4.

The parametric study begins with the consolidation analysis, in order to check the initial vertical effective stress in the soil after the foundation is built on the seabed. Then, the WSSI analysis is performed. The wave-induced seabed response around the structure is investigated. Finally, liquefaction assessment is performed with a comparison of two liquefaction criteria. Results and discussions are as follows.

5.2.1. *Consolidation*

When the structure is built on the seabed, the gravitational forces will induce a gradual dissipation of the excess pore pressure and a compression of the soil skeleton. The effective stress distribution in the surrounding soil will be significantly changed. According to the 1D Terzaghi's consolidation theory, the time for completing 90% consolidation can be expressed as (Wang, 2017):

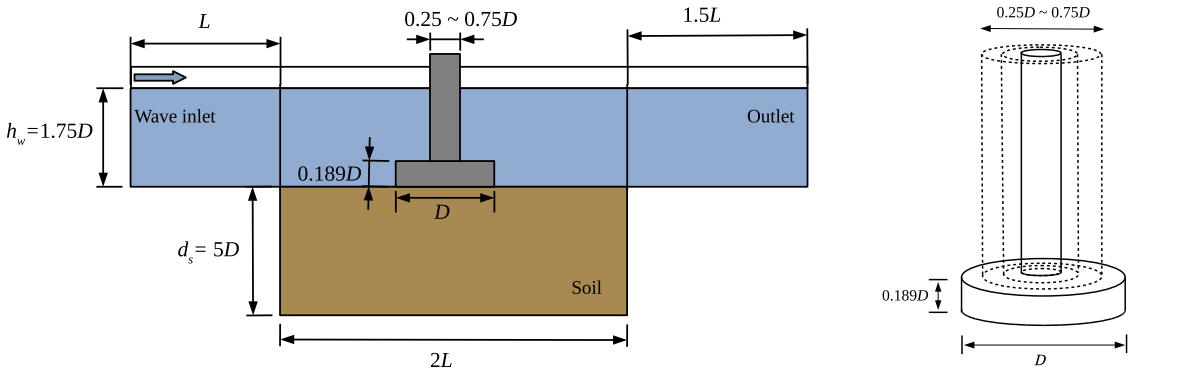

(a) Numerical layout of wave-structure-seabed interaction. (b) Geometries of the structures.

Fig. 14. Numerical models of the parametric study.

Table 4
Parameter settings of the parametric study of wave-structure-seabed interaction. D is the characteristic diameter of the foundation slab with $D = 1$ in the present parametric study.

Wave parameters			
Water depth h_w (m)	1.75D		
Wave height H (m)	0.95D		
Wave length L (s)	10D		
Wave period T (m)	2.6 s for $D = 1$		
Structure parameters			
Characteristic length D (m)	1		
Bottom slab height h_b (m)	0.189D		
Shaft diameter $D^{'}$ (m)	0.25–0.75D		
Density ρ (kg/m^3)	2400		
Young's modules (N/m^2)	2.2×10^{10}		
Poisson's ratio	0.2		
Seabed parameters			
Seabed thickness d_s (m)	5D		
Young's modules (N/m^2)	$E_x = 1.2 \times 10^7$	$E_y = 1.2 \times 10^7$	$E_z = 2 \times 10^7$
Poisson's ratios	$\nu_{xy} = 0.2$	$\nu_{yz} = 0.24$	$\nu_{zx} = 0.4$
Permeabilities (m/s)	$k_x = 0.0005$	$k_y = 0.0005$	$k_z = 0.0001$
Saturation factor S_r	0.975		
Porosity n	0.3		

$$t_{90} = T_v \frac{H_d^2}{c_v} \tag{33}$$

where H_d is the drainage distance of the layer, $T_v = 0.848$ is the vertical consolidation time factor for 90% consolidation, c_v is the consolidation coefficient calculated by

$$c_v = \frac{2Gk_z(1-\nu)}{\gamma_w(1-2\nu)} \tag{34}$$

where k_z is the vertical permeability and γ_w is the bulk specific weight of the pore water. In the present consolidation analysis, the gravitational force of the foundation reduced by the buoyant force is applied on the interface between the structure bottom and the seabed. Fig. 15 presents the distribution of the vertical effective stresses $\sigma_z^{'}$ and the vertical soil displacement U_z in the soil when the consolidation process is completed. A negative value of $\sigma_z^{'}$ indicates the compression of the soil skeleton. During the long-time consolidation, the gravity force from the foundation is gradually transferred to the supporting soil skeleton. It shows that below the foundation, the vertical effective stress and soil displacement are both amplified compared to those at the far field. Fig. 16 shows the vertical effective stress and the vertical displacement on horizontal lines. The red curves are the $\sigma_{z0}^{'}$ and U_z at the seabed surface. It is seen that after the completion of the consolidation, the vertical effective stress at the seabed surface beside the foundation becomes zero. Below the structure bottom, the vertical effective stress is a constant of $(W - B)/A$. In a deeper soil, the effective stress (shown as the blue dashed curve in Fig. 16a) is higher than that at the seabed surface since the gravity force is transferring downward. On the other hand, the vertical soil displacement U_z is gradually decreasing in a deeper seabed and the maximum deformation is right beneath the center of the structure bottom.

5.2.2. WSSI analysis

After the consolidation analysis, the steep waves are simulated to propagate over the seabed. Fig. 17 presents the wave elevation and the dynamic wave pressure on the seabed at locations upstream to the foundation with 5D and 1D distance to the foundation center (i.e., $x/D = -5$ and $x/D = -1$). It is shown that for the foundation with $D^{'}/D = 0.25$, the wave elevation at $x/D = -1$ is just slightly higher than that at $x/D = -5$, so does the dynamic wave pressure on the seabed. With $D^{'}/D = 0.5$, the difference is still not significant. When $D^{'}/D$ continuously increases to 0.75, both wave crest and wave trough become visibly steeper at $x/D = -1$ and the wave amplitude increases. Fig. 17 also shows the wave elevation and seabed pressure with $D^{'}/D = 1$, where the wave crest becomes sharper and the pressure amplitude at $x/D = -1$ is apparently higher than that at $x/D = -5$. A larger $D^{'}/D$ will apparently increase the wave reflection in the near field of the foundation and also the wave pressure on the seabed near the foundation slab. When waves further approaches the structure, the wave elevation is even more increased. However, the initial vertical effective stress in the seabed close to the structure will also be very high because of the consolidation process, so that the liquefaction may not happen. Thereby, the WSSI analysis and following liquefaction analysis focuses on the location with a 0.5D distance to the slab surface, e.g. $x/D = -1$ in Fig. 17.

In the present study, the structure is considered as a medium which transfers the wave effect to the seabed. Previous studies assumed a uniform structural force on the seabed or consider the structure and the seabed as the same type of porous media (Ulker et al., 2010; Ye, 2012b; Ye et al., 2013a). However, in the present study, the structure and the seabed are treated as independent systems. Therefore, the effect of the structure as a medium which transfers the wave effect to the seabed can be assessed. The wave-induced structural response is solved by a linear elastic structure solver to obtain the instantaneous structural stress at the structure-seabed interface. The structural shear stress tensor $\boldsymbol{\sigma}$ at the structure bottom is then imposed on the seabed as a time-varying

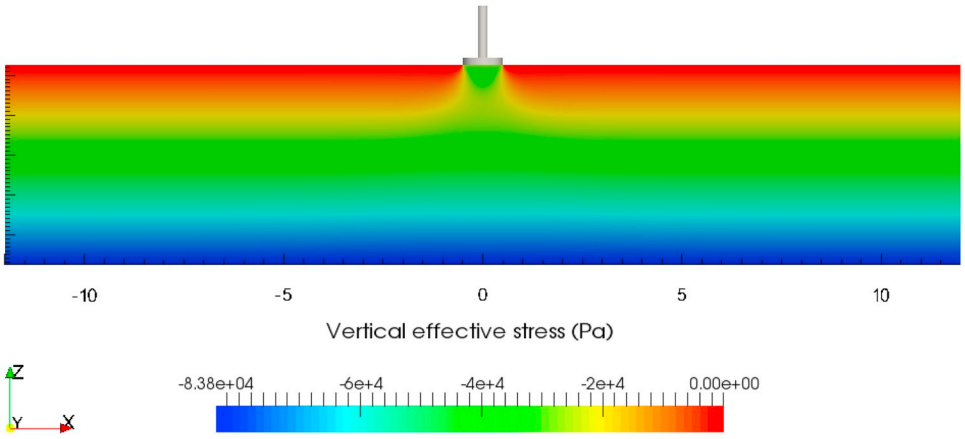

(a) Initial vertical soil effective stress $\sigma_{z0}^{'}$ (Pa) after the completion of the consolidation.

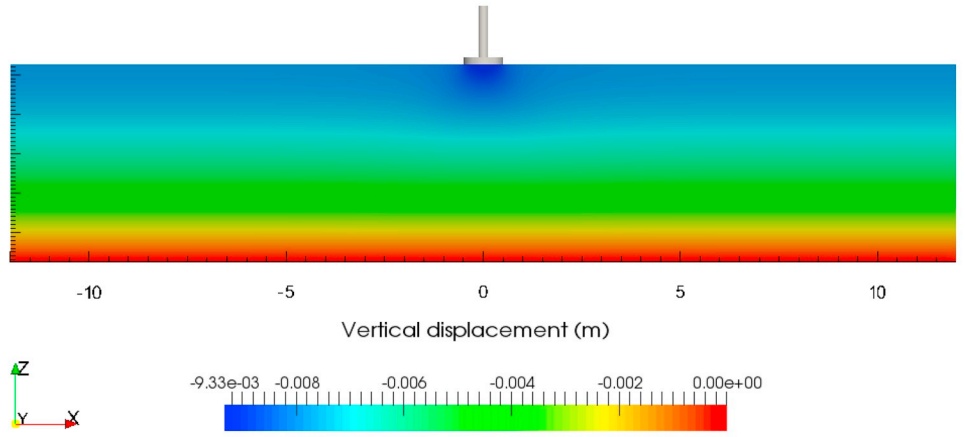

(b) Vertical soil displacement U_z (m) after the completion of the consolidation.

Fig. 15. Soil condition after the completion of the consolidation.

boundary condition. Fig. 18 and Fig. 19 present the distributions of dynamic wave pressure and wave velocity in the wave domain, as well as the distributions of vertical effective stress and vertical displacement in the soil domain when wave crest is reaching the foundations with $D^{'}/D = 0.5$ and 0.75. At this moment, a wave crest with high velocity is reaching the upstream side of the foundation, causing high pressure on the upstream side of the foundation and low pressure on the downstream side of the foundation. The foundation is experiencing a tilting force towards its downstream side at this instantaneous moment. To balance this tilting force, the foundation is compressing the soil at its downstream side and releasing the soil at its upstream side from the compression. In the soil, it is seen in Figs. 18a and 19a that the vertical effective stress under the structure bottom has opposite signs to its surrounding soil. The wave velocity field and the vertical soil displacement are shown in Figs. 18b and 19b. It is seen that the wave crest contains the highest wave velocity. When the wave crest is approaching to the structure, the soil beneath the downstream side of the foundation is compressed with a negative vertical displacement. Meanwhile, the soil beneath the upstream side of the foundation is released from the compression. On the contrary, when the wave trough approaches the foundation, it causes tension force in the seabed upstream to the foundation. A tension force can trigger liquefaction in the soil. However, at the same time, the structure experiences a tilting force towards its upstream side so that it causes compression force in the upstream nearby soil. Therefore, the wave-induced structural stress can have a mitigating effect on the momentary liquefaction in the soil very close to the foundation bottom. Fig. 19a also shows that with $D^{'}/D = 0.75$, the effect of the wave-induced structural stress on the underneath soil is stronger than that with $D^{'}/D = 0.5$ in Fig. 18a.

Fig. 20 shows the transient pore pressure and seepage flow in the seabed at the time instant of t/T = 9.45. The arrows in the seabed denote the vector of the pore pressure gradient, illustrating the seepage flow in the physical behavior. It is seen that at this time instant, wave trough is passing the foundation. The pressure gradient triggers notable upward seepage flows in the vicinity of the foundation. Once the upward seepage forces exceed the initial vertical effective stress, the momentary liquefaction will occur and influence the safety of the foundation. It is also seen that the dynamic waves only affect a certain depth of the seabed. The excess pore pressure vanishes in a deeper soil skeleton.

5.2.3. *Liquefaction*

For 1D quasi-static Biot's model, the criterion based on the excess pore pressure and that based on the vertical effective stress should lead to the same result (Sumer, 2014b), since the vertical effective stress $\sigma_z^{'}$ is theoretically the same as $p - p_b$ due to the force balance in the vertical direction. However, for the present 3D partial dynamic Biot's model with inertia force of the soil skeleton, the two criteria will lead to different assessment results. Fig. 21 shows the maximum liquefaction depths d_L in a wave cycle along the x-axis evaluated by 3D liquefaction criteria modified from Okusa (1985) and Zen and Yamazaki (1990b) (criterion A and B), respectively. The maximum liquefaction depths around foundations in different $D^{'}/D$ are compared. It is seen that as $D^{'}/$

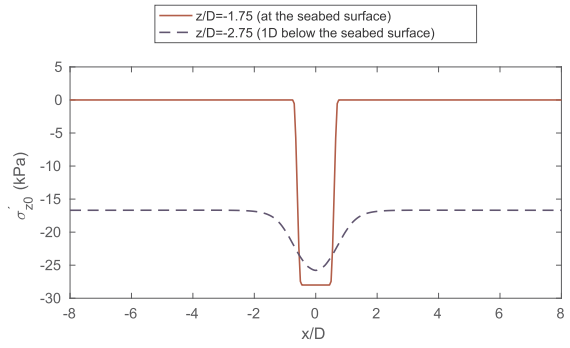

(a) Vertical soil effective stress σ'_{z0} (Pa) along horizontal lines in the seabed.

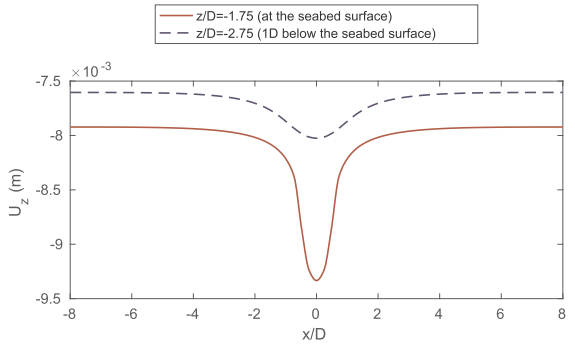

(b) Vertical soil displacement U_z (m) along horizontal lines in the seabed.

Fig. 16. Soil condition after the completion of the consolidation along the horizontal lines: $y/D = 0, z/D = -1.75$ and $y/D = 0, z/D = -2.75$.

D increases from 0.25 to 0.75, the liquefaction risk in terms of the maximum liquefaction depth and the liquefaction amplified distance near the foundation generally increases. The dashed line is the maximum liquefaction depth with $D'/D = 1$, providing an upper limit reference for the present parametric study. In a dimensional case, for a gravity-based foundation with a slab diameter D of 19 m and a shaft parameter D' of 9.5 m as an example, the maximum liquefaction depth at the given steep wave condition can reach 2.4 m.

For both criteria A and B, the highest liquefaction risk happens at a location of $x/D = -1 \pm 0.25$ upstream to the foundation. It is because that the liquefaction risk is determined by two factors, i.e., the wave effect and the initial vertical effective stress in the soil. As waves propagate to the foundation, the dynamic wave pressure is increasing due to the decreasing of the wave velocity when approaching to the foundation, according to the Bernoulli equation. The increase of the wave pressure and further the pore pressure gradient in the seabed will cause a higher liquefaction risk in the seabed. However, at the same time, the initial vertical effective stress in the seabed also increases when approaching to the foundation. The increase of the initial vertical effective stress will cause a lower liquefaction risk in the seabed. Two factors have opposite effect on the liquefaction risk as getting closer to the foundation. It is observed in Fig. 21 that the wave effect is dominant at $x/D = -1.25$ to -0.75 and the initial vertical effective stress is dominant at $x/D = -0.75$ to -0.5. When it is very close to the foundation slab ($x/D = \pm 0.5$), the initial vertical effective stress due to the consolidation is very high so that the liquefaction would not happen near the slab surface. At the downstream of the structure, the maximum liquefaction depths predicted by criterion A are the same for all D'/D, while criterion B gives a higher prediction of maximum liquefaction depths with $D'/D = 1$.

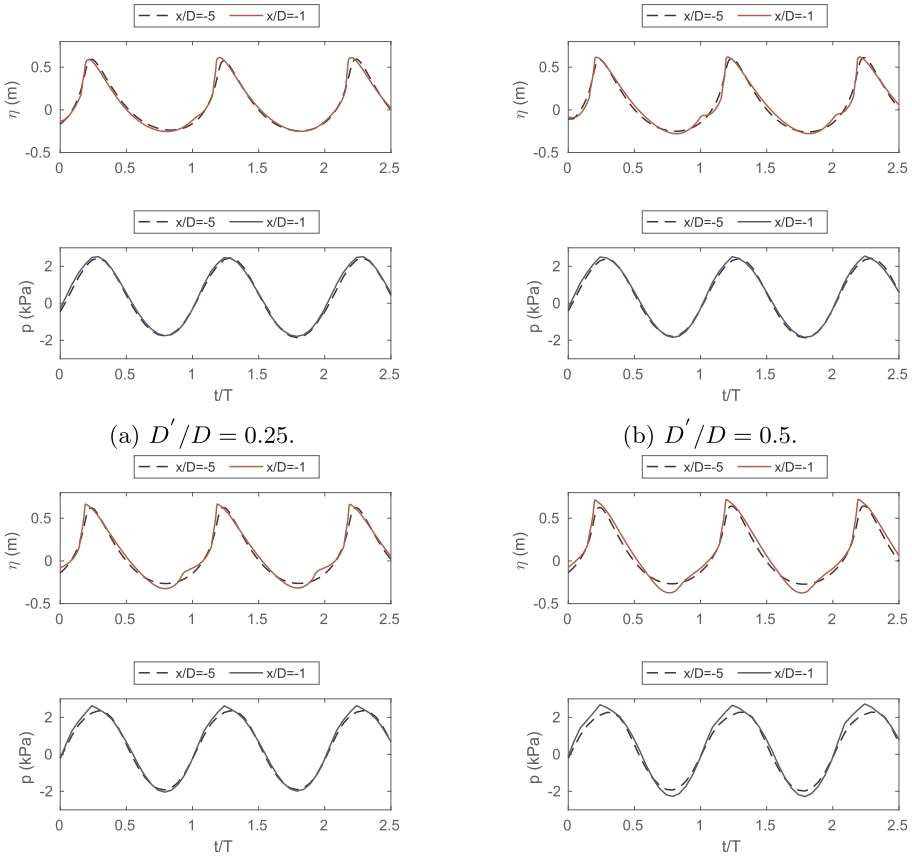

(a) $D'/D = 0.25$. (b) $D'/D = 0.5$.

(c) $D'/D = 0.75$. (d) $D'/D = 1$.

Fig. 17. Surface elevation and wave pressure on the seabed at a far-field location and a near-field location to the structure.

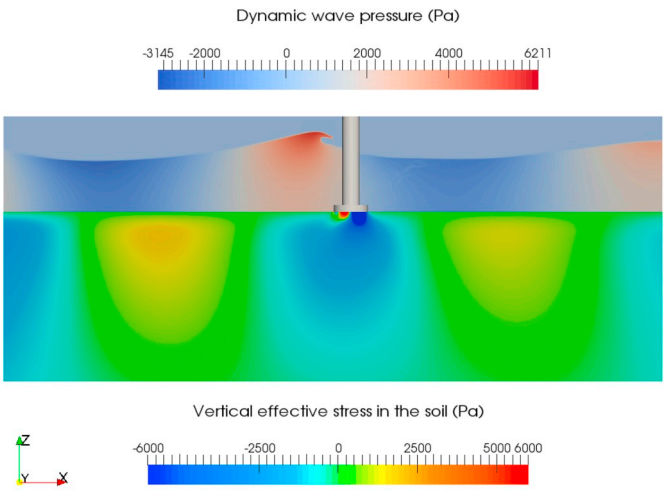

(a) Dynamic wave pressure and vertical effective stress in the soil.

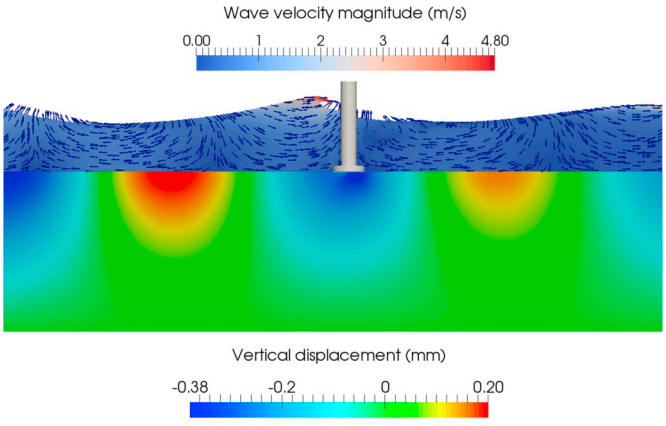

(b) Wave velocity and vertical soil displacement.

Fig. 18. Wave crest approaches the structure with $D^{'}/D = 0.5$ and generate high opposite vertical stress beneath the structure bottom σ_z (Pa) compared to the nearby field.

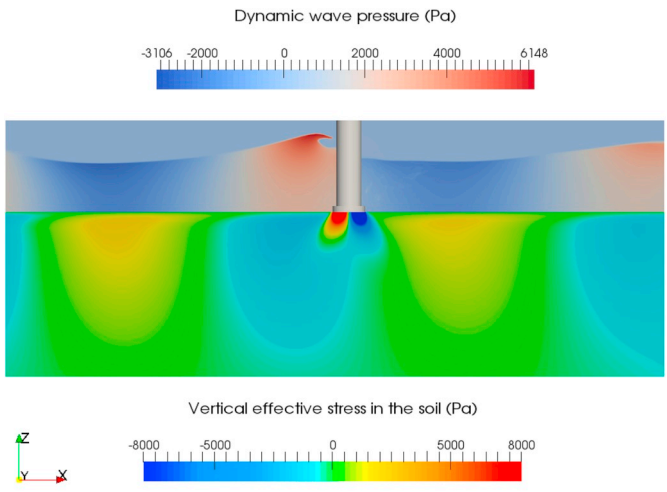

(a) Dynamic wave pressure and vertical effective stress in the soil.

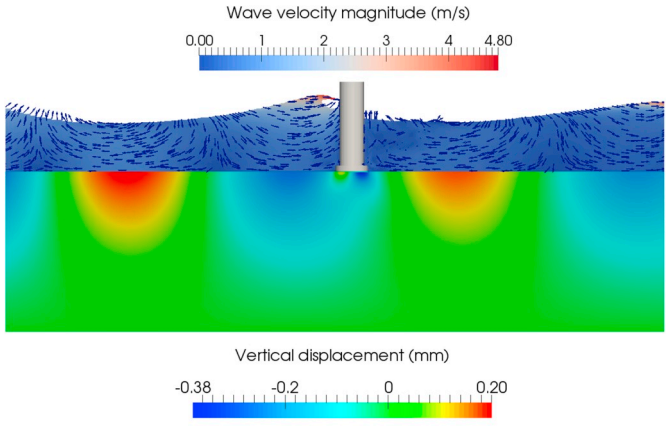

(b) Wave velocity and vertical soil displacement.

Fig. 19. Wave crest approaches the structure with $D^{'}/D = 0.75$ and generate high opposite vertical stress beneath the structure bottom σ_z (Pa) compared to the nearby field.

The maximum liquefaction depths d_L around the foundation from 0 to 360° in a circle with $r/D = 1$ (i.e., $0.5D$ to the slab surface) is investigated, as shown in Fig. 22. It appears that the upstream side has a higher liquefaction depth than the downstream side. It is general found that the upstream side of the offshore foundation is more vulnerable to the liquefaction risk (also seen in the work of Lin et al. (2017) and Li et al. (2018)), therefore needs more protection. Chang and Jeng (2014) investigated the liquefaction protection methodology and they suggested to replace the existing layers of the surrounding soil with higher permeability materials to reduce the liquefaction risk. In the engineering practice, gravity-based structures are usually fitted with skirts to prevent the hydraulic process of scour channels penetrating underneath the structure, which can also be helpful to prevent the seepage flow penetration and further liquefaction risk around the foundations. Based on the parametric study, it is found that the design of a smaller $D^{'}/D$ is able to alleviate the liquefaction risk around the foundation in the steep coastal waves.

It appears that criterion A and B provide similar results of maximum liquefaction distribution. However, criterion B based on the excess pore pressure (modified from Zen and Yamazaki (1990b)) gives relatively higher liquefaction risk prediction than criterion A based on the effective stress (modified from Okusa (1985)). Also, the length of the amplified liquefaction zone predicted by criterion B is larger than that predicted by criterion A. Criterion B can be a better choice for engineering design since it provides more conservative solution.

6. Conclusions

An open-source CFD toolbox for simulating the wave-induced seabed response and liquefaction around the marine structures including the consolidation analysis, WSSI analysis, and liquefaction assessment has been presented in the present work. The whole model is implemented in the FVM-based OpenFOAM framework. The coupling between the multiphysics is achieved by the data interpolating and mapping via the common boundaries. The FV partial dynamic soil model is modified from Biot's consolidation theory accounting for the anisotropic seabed properties.

The present model has been verified and validated against the theoretical solution and experimental data. The consolidation solver is verified by the analytical solution for the one-dimensional Terzaghi's consolidation test (Terzaghi, 1944; Wang, 2017). The dynamic wave-induced seabed response solver is validated against the experimental data of standing wave-induced pore pressure under a vertical wall (Tsai and Lee, 1995). The integrated WSSI model is validated against the wave data and soil pore pressure data of a wave-pile-soil interaction experiment (Qi and Gao, 2014; Qi, 2018). Two case

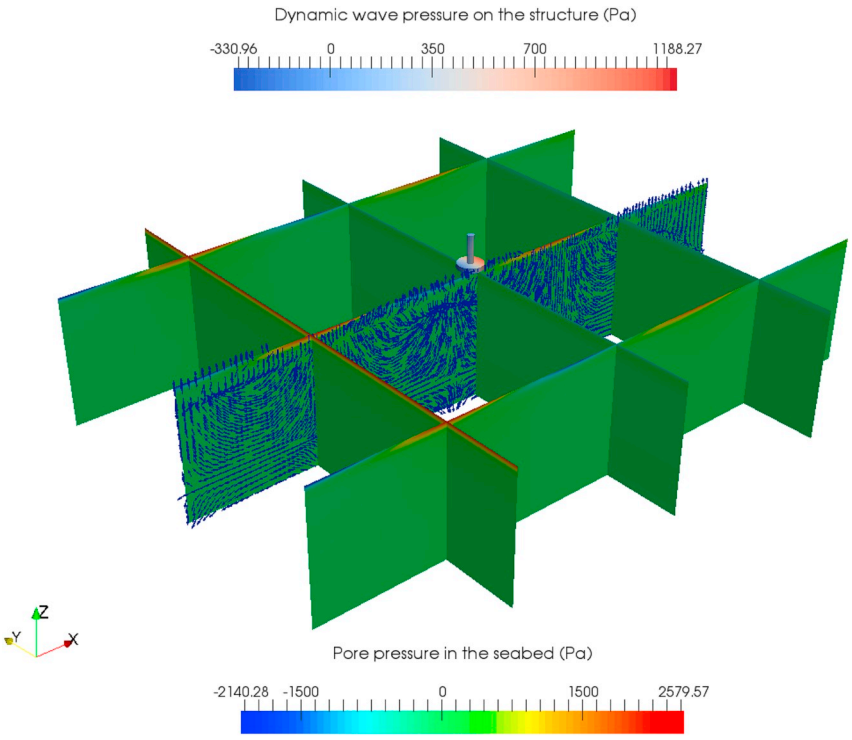

Fig. 20. Transient pore pressure and seepage flow at the time of t/T = 9.45.

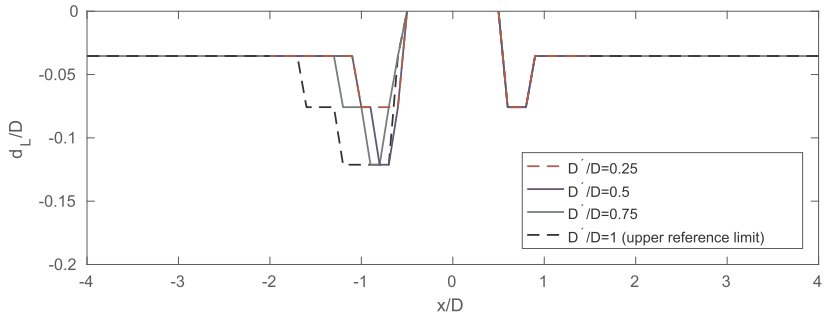

(a) Evaluated by liquefaction criterion A modified from Okusa (1985) based on the effective stress.

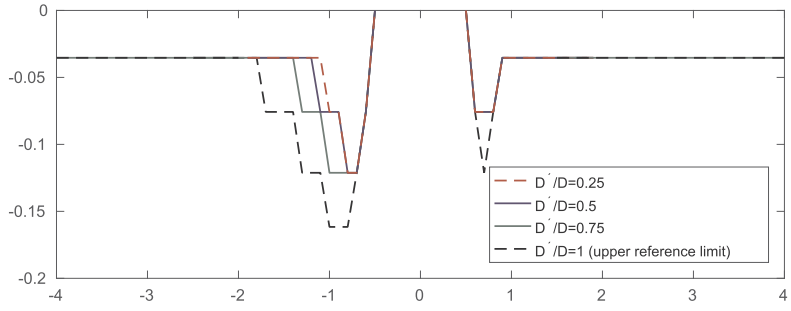

(b) Evaluated by liquefaction criterion B modified from Zen & Yamazaki (1990b) based on the excess pore pressure.

Fig. 21. Maximum liquefaction depths in a wave cycle beside the foundation along x-axis. The curves are plotted with sampled points at every x/D = 0.1.

studies have been conducted in the present work in terms of the analysis of 2D nonlinear wave-soil interaction and the investigation of 3D wave-structure-seabed interaction around gravity-based foundations. For the latter case study, a systematic investigation process including consolidation analysis, wave-induced seabed response and liquefaction assessment has been performed. Two liquefaction criteria based on the effective stress and based on the excess pore pressure have been applied and compared. It is recommended to use the criteria modified from Zen and Yamazaki (1990b) based on the excess pore pressure as it provides more conservative solution for evaluating the liquefaction risk around

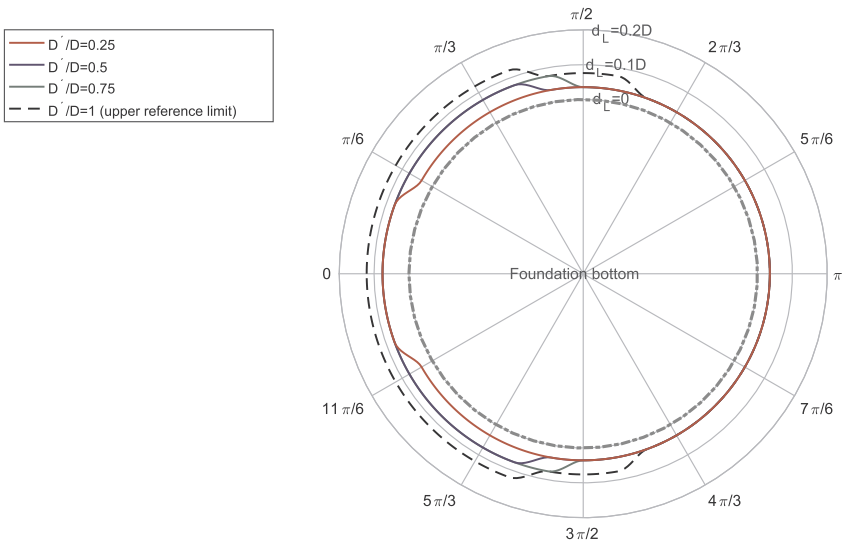

(a) Evaluated by liquefaction criterion A modified from Okusa (1985) based on the effective stress.

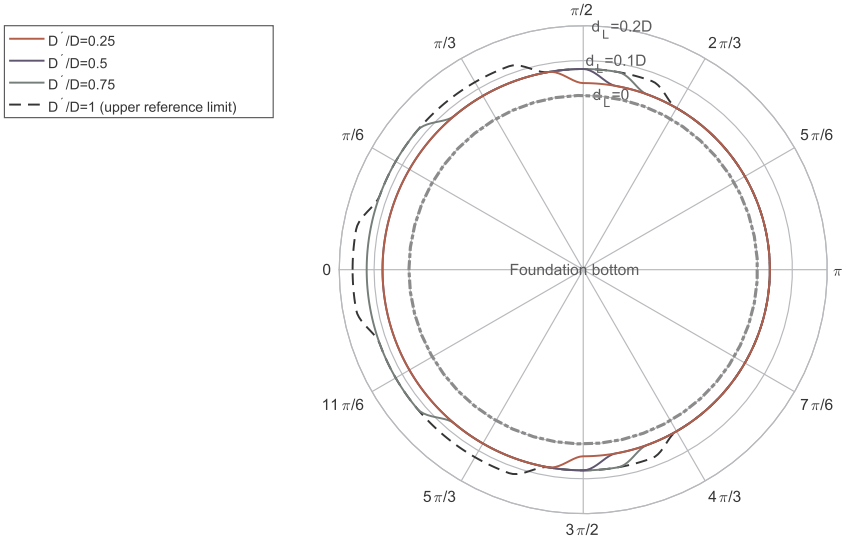

(b) Evaluated by liquefaction criterion B modified from Zen & Yamazaki (1990b) based on the excess pore pressure.

Fig. 22. Maximum liquefaction depth in a wave cycle around the foundation bottom with a distance of 0.5*D* to the slab surface.

the offshore foundations.

The present model can be applied to the seabed response analysis around the marine structures and offshore foundations in various wave conditions, providing safety assessment based on the practical assumptions. The present toolbox in the FVM-based OpenFOAM framework allows structured and unstructured meshing for either simple or complex geometries. The segregated approach and parallelism provide a fast and memory-efficient solution to certain coastal and offshore engineering problems.

Acknowledgment

This study was supported in part with computational resources provided by the Norwegian Metacenter for Computational Science (NOTUR), under Project No: NN9372K. The authors acknowledge Dr. Wen-Gang Qi from Chinese Academy of Sciences for providing the experimental data.

References

Berberović, E., van Hinsberg, N.P., Jakirlić, S., Roisman, I.V., Tropea, C., 2009. Drop impact onto a liquid layer of finite thickness: dynamics of the cavity evolution. Physical Review E 79, 036306.
Biot, M.A., 1941. General theory of three-dimensional consolidation. J. Appl. Phys. 12, 155–164.
Biot, M.A., 1956. Theory of propagation of elastic waves in a fluid-saturated porous solid. ii. higher frequency range. J. Acoust. Soc. Am. 28, 179–191.
Chang, K.-T., Jeng, D.-S., 2014. Numerical study for wave-induced seabed response around offshore wind turbine foundation in donghai offshore wind farm, shanghai, China. Ocean. Eng. 85, 32–43.
Dean, R.G., 1965. Stream function representation of nonlinear ocean waves. J. Geophys. Res. 70, 4561–4572.
Demirdžić, I., Horman, I., Martinović, D., 2000. Finite volume analysis of stress and deformation in hygro-thermo-elastic orthotropic body. Comput. Methods Appl. Mech. Eng. 190, 1221–1232.
Demirdžić, I., Martinović, D., 1993. Finite volume method for thermo-elasto-plastic stress analysis. Comput. Methods Appl. Mech. Eng. 109, 331–349.
Demirdžić, I., Muzaferija, S., 1994. Finite volume method for stress analysis in complex domains. Int. J. Numer. Methods Eng. 37, 3751–3766.
Elsafti, H., Oumeraci, H., 2016. A numerical hydro-geotechnical model for marine gravity structures. Comput. Geotech. 79, 105–129.

Esteban, M., Couñago, B., López-Gutiérrez, J., Negro, V., Vellisco, F., 2015. Gravity based support structures for offshore wind turbine generators: Review of the installation process. Ocean. Eng. 110, 281–291.
Fenton, J.D., 1985. A fifth-order Stokes theory for steady waves. J. Waterw. Port, Coast. Ocean Eng. 111, 216–234.
Gatmiri, B., 1990. A simplified finite element analysis of wave-induced effective stresses and pore pressures in permeable sea beds. Geotechnique 40, 15–30.
Higuera, P., Lara, J.L., Losada, I.J., 2013. Realistic wave generation and active wave absorption for Navier–Stokes models: application to openfoam®. Coast. Eng. 71, 102–118.
Jacobsen, N.G., Fuhrman, D.R., Fredsøe, J., 2012. A wave generation toolbox for the open-source cfd library: openfoam®. Int. J. Numer. Methods Fluids 70, 1073–1088.
Jasak, H., Weller, H., 2000. Application of the finite volume method and unstructured meshes to linear elasticity. Int. J. Numer. Methods Eng. 48, 267–287.
Jeng, D., Hsu, J., 1996. Wave-induced soil response in a nearly saturated sea-bed of finite thickness. Geotechnique 46, 427–440.
Jeng, D.-S., 1997. Wave-induced seabed instability in front of a breakwater. Ocean. Eng. 24, 887–917.
Jeng, D.-S., 1998. Wave-induced seabed response in a cross-anisotropic seabed in front of a breakwater: an analytical solution. Ocean. Eng. 25, 49–67.
Jeng, D.-S., 2012. Porous Models for Wave-Seabed Interactions. Springer Science & Business Media, pp. 13–17.
Jeng, D.-S., Cha, D., 2003. Effects of dynamic soil behavior and wave non-linearity on the wave-induced pore pressure and effective stresses in porous seabed. Ocean. Eng. 30, 2065–2089.
Jeng, D.-S., Lin, Y.-S., 2000. Poroelastic analysis of the wave–seabed interaction problem. Comput. Geotech. 26, 43–64.
Jeng, D.-S., Rahman, M., 2001. Wave-induced oscillatory soil response: difference between quasi-static and dynamic solutions. Computer Methods and Advances in Geomechanics 2, 1103–1106.
Jeng, D.-S., Ye, J.-H., Zhang, J.-S., Liu, P.-F., 2013. An integrated model for the wave-induced seabed response around marine structures: model verifications and applications. Coast. Eng. 72, 1–19.
Jeppsson, J., Larsen, P.E., Larsson, Å., 2008. Technical Description Lillgrund Wind Power Plant. Vattenfall Vindkraft AB. Lillgrund Pilot Project.
Kjekstad, O., Lunne, T., 1981. Soil parameters used for design of gravity platforms in the north sea. Appl. Ocean Res. 3, 50–58.
Li, Y., 2016. Implementation of multiple time steps for the multi-physics solver based onchtmultiregionfoam. In: Nilsson, H. (Ed.), CFD with OpenSource Software, 2016. Chalmers University of Technology.
Li, Y., Ong, M.C., Tang, T., 2018. Numerical analysis of wave-induced poro-elastic seabed response around a hexagonal gravity-based offshore foundation. Coast. Eng. 136, 81–95.
Li, Y., Ong, M.C., Tang, T., 2019. https://github.com/liyzpearl/elasticsoilsolvers.
Lin, Z., Pokrajac, D., Guo, Y., Jeng, D.-S., Tang, T., Rey, N., Zheng, J., Zhang, J., 2017. Investigation of nonlinear wave-induced seabed response around mono-pile foundation. Coast. Eng. 121, 197–211.
Liu, X., García, M.H., Muscari, R., et al., 2007. Numerical investigation of seabed response under waves with free-surface water flow. Int. J. Offshore Polar Eng. 17.
Okusa, S., 1985. Wave-induced stresses in unsaturated submarine sediments. Geotechnique 35, 517–532.
Qi, W.-G., 2018. Personal Communication by Email.
Qi, W.-G., Gao, F.-P., 2014. Physical modeling of local scour development around a large-diameter monopile in combined waves and current. Coast. Eng. 83, 72–81.
Raman-Nair, W., Sabin, G.C.W., Biot, Mohr, Coulomb, 1991. Wave-induced failure of poroelastic seabed slopes: a boundary element study. Proc. Inst. Civ. Eng. 91, 771–794.
Sui, T., Zhang, C., Guo, Y., Zheng, J., Jeng, D.-S., Zhang, J., Zhang, W., 2016. Three-dimensional numerical model for wave-induced seabed response around mono-pile. Ships Offshore Struct. 11, 667–678.
Sui, T., Zhang, C., Jeng, D.-s., Guo, Y., Zheng, J., Zhang, W., Shi, J., 2019. Wave-induced seabed residual response and liquefaction around a mono-pile foundation with various embedded depth. Ocean. Eng. 173, 157–173.
Sui, T., Zheng, J., Zhang, C., Jeng, D.-S., Zhang, J., Guo, Y., He, R., 2017. Consolidation of unsaturated seabed around an inserted pile foundation and its effects on the wave-induced momentary liquefaction. Ocean. Eng. 131, 308–321.
Sumer, M., 2014. Liquefaction Around Marine Structures. World Scientific Publishing Company, pp. 54–55 (chapter 3).
Sumer, M., 2014. Liquefaction Around Marine Structures. World Scientific Publishing Company, pp. 151–152 (chapter 4).
Tang, T., Johannesson, B., Roenby, J., 2014. An integrated fvm simulation of wave-seabed-structure interaction using openfoam. In 9th OpenFOAM Workshop 23–26. June 2014 in Zagreb, Croatia.
Terzaghi, K., 1944. Theoretical Soil Mechanics. Chapman And Hali, Limited John Wiler And Sons, Inc, New York.
Tsai, C., 1995. Wave-induced liquefaction potential in a porous seabed in front of a breakwater. Ocean. Eng. 22, 1–18.
Tsai, C.-P., Lee, T.-L., 1995. Standing wave induced pore pressures in a porous seabed. Ocean. Eng. 22, 505–517.
Ulker, M., Rahman, M., Guddati, M., 2009. Breaking wave-induced dynamic response of rubble mound and seabed under a caisson breakwater. In: ASME 2009 28th International Conference on Ocean, Offshore and Arctic Engineering. American Society of Mechanical Engineers, pp. 141–150.
Ulker, M., Rahman, M., Guddati, M., 2010. Wave-induced dynamic response and instability of seabed around caisson breakwater. Ocean. Eng. 37, 1522–1545.
Ulker, M., Rahman, M., Jeng, D.-S., 2009. Wave-induced response of seabed: various formulations and their applicability. Appl. Ocean Res. 31, 12–24.
Vafai, K., Tien, C., 1981. Boundary and inertia effects on flow and heat transfer in porous media. Int. J. Heat Mass Transf. 24, 195–203.
Wang, H.F., 2017. Theory of Linear Poroelasticity with Applications to Geomechanics and Hydrogeology. Princeton University Press, pp. 124–128 (chapter 6).
Ye, J., 2012. 3D liquefaction criteria for seabed considering the cohesion and friction of soil. Appl. Ocean Res. 37, 111–119.
Ye, J., 2012. Numerical Analysis of Wave-Seabed-Breakwater Interactions. Ph.D. thesis. University of Dundee.
Ye, J., Jeng, D.-S., Liu, P.-F., Chan, A., Ren, W., Changqi, Z., 2014. Breaking wave-induced response of composite breakwater and liquefaction in seabed foundation. Coast. Eng. 85, 72–86.
Ye, J., Jeng, D.-S., Wang, R., Zhu, C., 2013. A 3-D semi-coupled numerical model for fluid–structures–seabed-interaction (FSSI-CAS 3D): model and verification. J. Fluids Struct. 40, 148–162.
Ye, J., Jeng, D.-S., Wang, R., Zhu, C., 2013. Validation of a 2-d semi-coupled numerical model for fluid–structure–seabed interaction. J. Fluids Struct. 42, 333–357.
Ye, J., Jeng, D.-S., Wang, R., Zhu, C., 2015. Numerical simulation of the wave-induced dynamic response of poro-elastoplastic seabed foundations and a composite breakwater. Appl. Math. Model. 39, 322–347.
Ye, J., Wang, G., 2015. Seismic dynamics of offshore breakwater on liquefiable seabed foundation. Soil Dyn. Earthq. Eng. 76, 86–99.
Ye, J., Wang, G., 2016. Numerical simulation of the seismic liquefaction mechanism in an offshore loosely deposited seabed. Bull. Eng. Geol. Environ. 75, 1183–1197.
Zen, K., Yamazaki, H., 1990. Mechanism of wave-induced liquefaction and densification in seabed. Soils Found. 30, 90–104.
Zen, K., Yamazaki, H., 1990. Oscillatory pore pressure and liquefaction in seabed induced by ocean waves. Soils Found. 30, 147–161.
Zhang, C., Zhang, Q., Wu, Z., Zhang, J., Sui, T., Wen, Y., 2015. Numerical study on effects of the embedded monopile foundation on local wave-induced porous seabed response. Math. Probl. Eng. 2015, 13, 184621.
Zhang, C., Zhang, Q., Zheng, J., Demirbilek, Z., 2017. Parameterization of nearshore wave front slope. Coast. Eng. 127, 80–87.
Zhao, H., Jeng, D.-S., Liao, C., Zhu, J., 2017. Three-dimensional modeling of wave-induced residual seabed response around a mono-pile foundation. Coast. Eng. 128, 1–21.
Zienkiewicz, O., Chang, C., Bettess, P., 1980. Drained, undrained, consolidating and dynamic behaviour assumptions in soils. Geotechnique 30, 385–395.